Chem Soc Rev

REVIEW ARTICLE

Check for updates

Cite this: DOI: 10.1039/c6cs00902f

Received 29th May 2017

DOI: 10.1039/c6cs00902f

rsc.li/chem-soc-rev

Recent advances in droplet wetting and evaporation

D. Brutin *[a,b] and V. Starov [c]

The wetting of solid surfaces using liquid droplets has been studied since the early 1800s. Thomas Young and Pierre-Simon Laplace investigated the wetting properties, as well as the role of the contact angle and the coupling of a liquid and solid, on the contact angle formation. The geometry of a sessile droplet is relatively simple. However, it is sufficiently complex to be applied for solving and prediction of real-life situations (for example, metallic inks for inkjet printing, the spreading of pesticides on leaves, the dropping of whole blood, the spreading of blood serum, and drying for medical applications). Moreover, when taking into account both wetting and evaporation, a simple droplet becomes a very complex problem, and has been investigated by a number of researchers worldwide. The complexity is mainly due to the physics involved, the full coupling with the substrate upon which the drop is deposited, the atmosphere surrounding the droplet, and the nature of the fluid (pure fluid, bi- or multi-phase mixtures, or even fluids containing colloids and/or nano-particles). This review presents the physics involved during droplet wetting and evaporation by focusing on the evaporation dynamics, the flow motion, the vapour behaviour, the surface tension, and the wetting properties.

1. Introduction

Studies on droplets and evaporation have been conducted over the past 50 years, resulting in the publication of more than 6800 papers (1967–2017) in referenced journals, as archived in the Scopus database. The total number of scientific publications has sharply increased over the same period for all areas of research in the area of life, health, and physical sciences. In total, the number of publications dealing with droplets and evaporation has multiplied by a factor of 10 during the last 50 years.

Several domains have been covered through this increase in publications. The distribution of publications in 2017 shows a

D. Brutin

David Brutin, PhD, Junior Fellow of the French University Insitut, Professor at Aix-Marseille University since 2015. He obtained his PhD in the field of mechanical engineering in 2003 at the University of Provence. Prof. Brutin is working on fluid mechanics, soft matter, energetic, and phase change heat transfer with pure and complex fluids. Prof. Brutin has published 50 research articles in recognized journals. Board member of two journals. Expert for several international funding agencies. In 2013, he co-organized the first Int. Workshop on Droplets. In 2015, he edited the first book on Droplets Wetting and Evaporation published by Elsevier.

V. Starov

Victor Starov, PhD, DSc, Fellow of the Royal Society of Chemistry, Professor at Chemical Engineering Department Loughborough University, UK; PhD from USSR Academy of Sciences on Capillary hysteresis in porous bodies; DSc degree form Sankt Petersburg University in Equilibrium and kinetics of thin liquid layers. Scientific interests: influence of surface forces on kinetics of wetting and spreading on solid and soft surfaces, kinetics of spreading over porous and hydrophobic surfaces; published more than 300 scientific papers. See a book V. Starov, M. Velarde, C. Radke "Wetting and Spreading Dynamics". Member of Editorial Board of 10 Journals.

---

[a] Aix-Marseille University, IUSTI UMR CNRS 7343, Marseille, France
[b] Institut Universitaire de France, IUF, Paris, France. E-mail: david.brutin@univ-amu.fr
[c] Loughborough University, Chemical Engineering Dept., UK. E-mail: v.m.starov@lboro.ac.uk

strong interest in mechanical and chemical engineering at more than 40%, fundamental physics and chemistry at 27%, material science at 10%, and energy applications at 7%. The energy field covers an increasing number of published papers dealing with droplets and evaporation, particularly because of certain applications including the printing of complex fluids, spray cooling, and DNA analysis.

This review is structured into five sections covering wetting and evaporation issues applied to sessile droplet configurations including both pure and complex fluids. Because the domain of sessile droplets is extremely wide, it is not easy to structure a review, present the theoretical concepts, and analyse the studies conducted by the scientific community. A droplet can be viewed from the perspective of chemists looking for wetting issues, colloid motions, and their influence on spreading and evaporation. The problem can also be addressed from a chemical/mechanical engineering point of view by looking at the internal flow motion or the vapour flow behaviour around an evaporating droplet. There are several ways to address this topic, which are summarized in Fig. 1. We address almost all of them in the following review.

The mind map shown in Fig. 2 provides the keywords used in this review. Each keyword is addressed in the review, and each branch corresponds to a sub-section; however, cross-links exist because the physics involved is strongly coupled with this area.

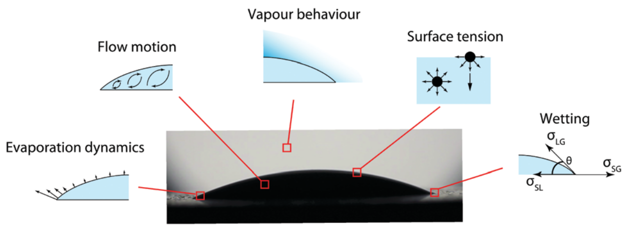
Vapour behaviour
Flow motion
Surface tension
Wetting
σ_{LG}
θ
σ_{SG}
σ_{SL}
Evaporation dynamics

Fig. 1 Ways to address the topic of droplet wetting and evaporation.[108]

Even in the simplest case of a pure liquid drop on an atomically flat substrate, many questions remain unanswered. Although it is well known that evaporation can by itself induce the formation of an apparent finite contact angle even for perfectly wetting liquids,[1] existing theories have yet to be validated under well-defined situations. In particular, only very recent theories include both the modification of apparent macroscopic contact angles, in the case of evaporation in an inert gas, as considered below, and the variation in contact angle owing to the contact line velocity.[2] These studies have shown that there is a non-negligible effect of the vapour cloud configuration on the induced contact angle. This vapour cloud, in turn, is heavily influenced by gravity currents owing to the large density of the vapour studied. The situation is further exacerbated by the fact that the rate of flux divergence at the contact line (moderated only by the microscopic effects within its close vicinity) and the associated phenomenon of evaporation-induced contact angles, even if local, nonetheless turn out to be rather sensitive to global currents. Clearly, all cases mentioned above do not favour producing a neat and reliable benchmark case, and therefore, an important motivation is to apply for microgravity conditions. No less essential is the fact that the presence of gravity typically increases the computation times by an order of magnitude, which can become a significant problem with expensive 3D computations and parametric studies. The existence of thermo-capillary instabilities occurring under evaporation in pure liquid droplets of ethanol under a reduced gravity environment has previously been described.[3] The use of parabolic flights has enabled this observation, but it is still insufficient in terms of the duration and residual acceleration to adequately conduct quantifiable measurements using infrared and visible light techniques and to apply accurate heat flux measurements. The problem is that the droplet interface is highly sensitive to the vibrations of the aircraft. A better level of microgravity and a longer duration of evaporation are needed.

The evaporation of a large liquid drop with a spherical cap on a rough surface certainly merits consideration for space

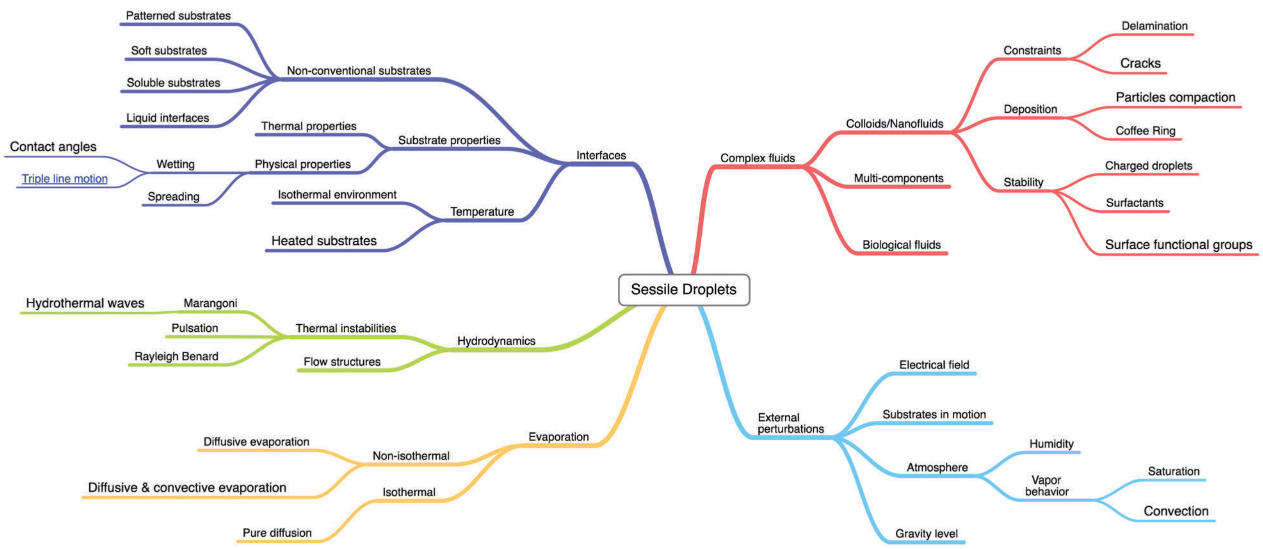
Sessile Droplets
Interfaces
Non-conventional substrates
Patterned substrates
Soft substrates
Soluble substrates
Liquid interfaces
Substrate properties
Thermal properties
Physical properties
Wetting
Contact angles
Triple line motion
Spreading
Temperature
Isothermal environment
Heated substrates
Hydrodynamics
Thermal instabilities
Marangoni
Hydrothermal waves
Pulsation
Rayleigh Benard
Flow structures
Evaporation
Non-isothermal
Diffusive evaporation
Diffusive & convective evaporation
Isothermal
Pure diffusion
Complex fluids
Colloids/Nanofluids
Constraints
Delamination
Cracks
Deposition
Particles compaction
Coffee Ring
Stability
Charged droplets
Surfactants
Surface functional groups
Multi-components
Biological fluids
External perturbations
Electrical field
Substrates in motion
Atmosphere
Humidity
Vapor behavior
Saturation
Convection
Gravity level

Fig. 2 Mind map and keywords used in the review.[108]

experiments, from both fundamental wettability and technological points of view. If a liquid drop is deposited on a rough surface, or on a textured surface where pillars are formed, then the contact states can be characterized using Wenzel or Cassie models. According to the Wenzel model, the liquid completely invades the texture, whereas according to the Cassie model, air is trapped at the contact: the former and latter characterise wetting and non-wetting states, respectively. It is known that a Cassie drop can be transformed into a Wenzel drop through external perturbations, such as vibration, for example. In particular, it has been revealed that the evaporation of a drop can induce the transition between the two states, as demonstrated in ref. 5. Understanding the physical mechanism of such transitions is important for a number of applications, which include the realization of robust super-hydrophobic states.

Although other effects have been studied, more data are required: for instance, the role of the thermal conductivity of the substrate. It has been shown that the evaporation rate of droplets on insulating substrates can be significantly lower. This is mainly due to the fact that the interfacial temperature of the drop decreases, particularly within the vicinity of the contact line. Examination of this phenomenon has therefore been planned through evaporation on both a highly conductive substrate (silicon/sapphire wafer) and on a poorly conducting substrate (glass wafer), and extracting the local evaporation rates and interfacial temperatures along the interface, with a comparison against numerical simulations and theoretical predictions. Further studies on the influence of Marangoni flows (thermal or solutal) on the drop shape and convection in a gas phase are also required. Finally, the influences of the roughness, chemical heterogeneity, and surface forces on the kinetics of evaporation are also important to understand because the different shapes of a disjoining pressure isotherm may result in completely different kinetics.[6]

In 2009, Bonn *et al.*[4] provided a comprehensive review of the current state of this area up to the year 2009. Below, the authors present an analysis of important problems that have appeared since then. In 2014, Sefiane[101] presented an extensive review of patterns from drying drops, and collected several keys papers describing the original patterns obtained after the droplets of a complex fluid are desiccated.

2. Wetting and spreading

2.1. Basics of wetting

Why do droplets of different liquids deposited on an identical solid substrate behave so differently (Fig. 3)? Moreover, why are the behaviours of identical droplets, for example, aqueous droplets, deposited on different substrates also so different? The generation of a uniform layer of mercury on a glass surface is impossible to achieve because the mercury layer will immediately form a droplet, which has a spherical cap with a contact angle of greater than 90° (Fig. 3). This case is referred to as a non-wetting case. Note that the contact angle is always measured inside the liquid phase (Fig. 3a–c). However, it is easy to make an oil layer (hexane or decane) on the same glass surface: for this purpose, an oil droplet can be deposited on the glass substrate, and the droplet will spread out completely (Fig. 3c). In this case, the contact angle decreases to zero over time.

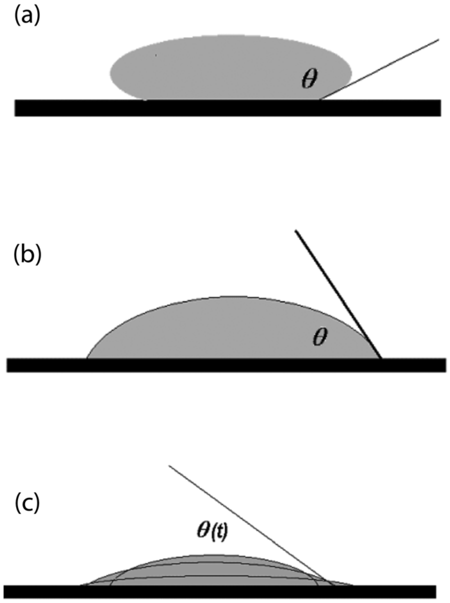

Fig. 3 Different wetting situations: (a) non-wetting case with a contact angle of greater than 90°. The examples are an aqueous droplet on Teflon and a mercury droplet on glass. (b) Partial wetting case with a contact angle between zero and 90°. The examples are an aqueous droplet on glass, mica, and metal. (c) Complete wetting case where the droplet spreads out completely and only a dynamic contact angle, $\theta(t)$, can be measured, which tends to reach zero over time, t. The examples are oil droplets on glass, mica, and metal, and aqueous droplets on a silicon wafer.

Using the same procedure but with an ordinary tap water droplet, an aqueous droplet deposited on an identical glass substrate spreads out only partially down to a contact angle of between zero and 90° (Fig. 3b). That is, an aqueous droplet on a glass surface shows behaviour between that of mercury and oil on an identical glass surface. These three cases (Fig. 3a–c) are referred to as non-wetting, partial wetting, and complete wetting, respectively.

Creating a water layer on a Teflon surface is also impossible for the exact reasons as mercury on a glass surface. That is, the same aqueous droplet can spread out partially on a glass substrate and does not spread at all on a Teflon substrate. The latter means that the wetting or non-wetting is not a property of the liquid only, but is a property of the liquid–solid pair.

In broader terms, complete wetting, partial wetting, and non-wetting behaviours are determined based on the nature of both the liquid and solid substrate. Considering Fig. 4, the three-phase contact line can be considered as where the three phases of liquid, solid, and vapour meet.

Consideration of the force balance in the tangential direction on the three-phase contact line results in the well-known Neumann–Young's rule, which connects the three interfacial tensions, γ_{sl}, γ_{sv}, and γ with the value of the equilibrium contact angle, θ_{NY}, (Fig. 4), where γ_{sl}, γ_{sv}, and γ are solid–liquid,

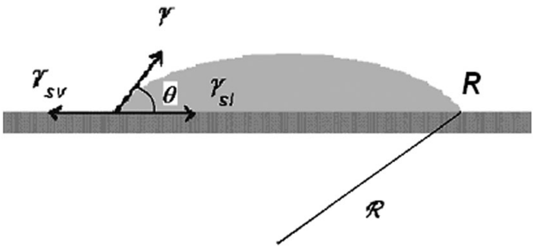

Fig. 4 Interfacial tensions at three-phase contact line. Here, $\Re$ is the radius of the droplet base, and $\Re$ is the radius of the droplet. The droplet is sufficiently small, and the gravity can be neglected.

solid–vapour, and liquid–vapour interfacial tensions, respectively (see ref. 7 for example):

$$\cos\theta_{\mathrm{NY}} = \frac{\gamma_{\mathrm{sv}} - \gamma_{\mathrm{sl}}}{\gamma} \tag{1}$$

Note that we marked the contact angle in eqn (1) as θ_{NY}, and we can see below that there is a good reason for doing so. In addition, eqn (1) has been deduced using the force balance in the tangential direction. Eqn (2) means there is no equilibrium in the normal direction, which is justified only for the case of a completely rigid substrate, and is not true for the case of a soft deformable substrate.

According to Fig. 4, the complete wetting case corresponds to a situation in which none of the forces can be compensated in the tangential direction at any contact angle, that is, if $\gamma_{\mathrm{sv}} > \gamma_{\mathrm{sl}} + \gamma$. A partial wetting case according to eqn (1) corresponds to $0 < \cos\theta_{\mathrm{NY}} < 1$, and finally, a non-wetting case corresponds to $-1 < \cos\theta_{\mathrm{NY}} < 0$. That is, eqn (1) reduces complete wettability, partial wettability, and non-wettability cases to the determination of three interfacial tensions, γ_{sl}, γ_{sv}, and γ. Everything appears to be easy and straightforward. Unfortunately, however, as we can see below, the situation is far more complex. First, is it possible to measure all three interfacial tensions γ_{sl}, γ_{sv}, and γ? There are a number of experimental methods for the measurements of liquid–vapour interfacial tension, γ (see for example ref. 7). Unfortunately, it is still impossible to directly measure γ_{sl} and γ_{sv} interfacial tensions. However, when applying Neumann–Young's rule (1), the situation is much worse. Recall that the pressure inside a spherical droplet (Fig. 4) is higher than the outside pressure. This difference shown below is referred to as excess equilibrium pressure,

$$P_{\mathrm{e}} = P_{\mathrm{out}} - P_{\mathrm{in}} = -\frac{\gamma}{\Re} < 0 \tag{2}$$

How many equilibrium states can a thermodynamic system have? The answer is one equilibrium (or quasi-equilibrium) state, or in certain cases, two or more separated from each other by potential barriers. According to eqn (1) the equilibrium contact angle does not depend on the droplet volume, and hence there is an infinite continuous set of equilibrium states that are not separated from each other by a potential barrier: Neumann–Young's equation does not specify the equilibrium volume of the droplet, V, or the excess pressure inside the drop, P_{e}, which can be any negative value. Both the volume of the droplet and the excess pressure can be arbitrary. The latter indicates that both the volume of the droplet and the pressure inside are not specified according to eqn (1): a droplet of any volume and pressure can be at equilibrium. This means the Neumann–Young equation in (1) is in drastic contradiction with thermodynamics. However, the error is definitely not in the derivation, which means we should return to the basics. At equilibrium, the following three conditions should hold:[2]

(a) The liquid in the droplet must be at equilibrium with its own vapour;

(b) the liquid in the droplet must be at equilibrium with the solid; and

(c) the vapour must be at equilibrium with the solid substrate.

The first requirement (a) results in equality of the chemical potentials of the molecules in the vapour and inside the droplet, which results in the following Kelvin equation for the excess pressure, P_{e}, inside the droplet:

$$P_{\mathrm{e}} = \frac{RT}{v_{\mathrm{m}}}\ln\frac{p_{\mathrm{s}}}{p} \tag{3}$$

where v_{m} is the molar volume of the liquid, p_{s} is the pressure of the saturated vapour at temperature T, R is the gas constant (which should not be confused with the radius of the drop base), and p is the vapour pressure at equilibrium with the liquid droplet. Eqn (3) determines the unique equilibrium of excess pressure P_{e}, and hence, according to eqn (2), the unique radius of the droplet (Fig. 4). We should recall here that the excess pressure inside the drop, P_{e}, is always negative (the pressure inside the droplet is larger than the pressure in the ambient air). This means that the right-hand side in eqn (3) should also be negative; however, the latter is possible only if $p > p_{\mathrm{s}}$, that is, the droplets can only be at equilibrium with an oversaturated vapour. This is a significant problem because the equilibration process continues for hours, and it is necessary to keep an oversaturated vapour over a solid substrate under investigation for a lengthy period of time with enormously high precision.[8] To the best of our knowledge, the latter is still beyond our experimental capabilities, which means it is difficult (if possible) to investigate experimentally the equilibrium of droplets on a solid substrate.

The main conclusion is that none of the droplets deposited on a solid substrate are at equilibrium with the surroundings under a saturated vapour, and are hence always in a state of evaporation, which is why droplet evaporation has attracted so much attention. Before starting a discussion on evaporation, it is important to understand the different stages of evaporation, and thus a brief introduction of the contact angle hysteresis is provided below.

2.2. Hysteresis of contact angle on smooth homogeneous solid surfaces through disjoining/conjoining pressure

The static hysteresis of the contact angle is usually attributed to the surface roughness and/or chemical heterogeneity. The traditional view of hysteresis based on chemical/topological heterogeneities was discussed by Bonn *et al.*[4] Although these properties of a solid substrate contribute substantially to the contact angle hysteresis, they are not the single reason. Convincing evidence of the presence of contact angle hysteresis even on a smooth homogeneous surface has been presented.[10–14] The most obvious example observed experimentally is the hysteresis of a liquid meniscus located in a thin free liquid film.[15–18] In this case, it is impossible to explain the hysteresis phenomenon through the presence of roughness and/or heterogeneity of the surface.

A theory of contact angle hysteresis of liquid droplets on smooth homogeneous solid surfaces was developed based on the surface forces and quasi-equilibrium phenomena[9,19] within the vicinity of the three-phase contact line. The developed theory was applied for calculations of the contact angle hysteresis in a capillary meniscus and droplet.[20,21] Contact angle hysteresis on a smooth homogeneous substrate appears in the case of partial wetting, where a disjoining/conjoining pressure isotherm has a characteristic s-shape as a result of a combination of the following:[22]

(1) The electrostatic component is caused through the formation of surface charges and an overlapping of electrical double layers, *i.e.*,

$$\Pi_E = RTc_0(\exp(\varphi) + \exp(-\varphi)) - 2RTc_0 - \frac{(RT)^2\varepsilon\varepsilon_0}{2F^2}\left(\frac{\partial\varphi}{\partial y}\right)^2, \tag{4}$$

where R, T, F, ε, and ε_0 are a universal gas constant, temperature in K, Faraday's constant, the dielectric constant of water, and the dielectric constant of a vacuum, respectively; c_0 is the electrolyte concentration; and y and φ are the coordinates normal to the liquid–air interface and the dimensionless electric potential in F/RT units, respectively.

The electric potential φ in eqn (1) is related to the surface charge density σ as[22]

$$\sigma_\mathrm{h} = \varepsilon\varepsilon_0\frac{RT}{F}\left(\frac{\partial\varphi}{\partial y}\right)_{y=h} \tag{5}$$

for the liquid–vapour interface, and

$$\sigma_\mathrm{s} = -\varepsilon\varepsilon_0\frac{RT}{F}\left(\frac{\partial\varphi}{\partial y}\right)_{y=0} \tag{6}$$

for the solid–liquid interface.

(2) The structural component is caused by a water molecule dipole orientation within the vicinity of the interfaces, and an overlapping of these structured layers. This component is presented as a combination of short- and long-range interactions:[23]

$$\Pi_\mathrm{S} = K_1\exp(-h/\lambda_1) + K_2\exp(-h/\lambda_2) \tag{7}$$

where K_1 and K_2, and λ_1 and λ_2, are parameters related to the magnitude and characteristic length of the structural forces, respectively. The indexes 1 and 2 correspond to the short- and long-range structural interactions, respectively. Currently, all latter four constants should be extracted from the experimental data.

(3) The molecular or van der Waals component is[22]

$$\Pi_\mathrm{M}(h) = \frac{A}{6\pi h^3} \tag{8}$$

where $A = -A_\mathrm{H}$ and A_H are the Hamaker constants. Note that the importance of the van der Waals component is usually grossly exaggerated in the literature. However, also note that with $\Pi_\mathrm{M}(h) \to \infty$ at $h \to 0$, the disjoining/conjoining pressure is a macroscopic value, which is valid only for a $h \gg$ molecular dimension. Under the latter condition, other components of the disjoining/conjoining pressure become equally or even more important than the van der Waals component in the case of an aqueous solution.

The resulting disjoining/conjoining pressure isotherm is[20–22]

$$\Pi(h) = \Pi_\mathrm{M}(h) + \Pi_\mathrm{E}(h) + \Pi_\mathrm{S}(h). \tag{9}$$

A schematic presentation of two possible shapes of disjoining/conjoining pressure isotherms is given in Fig. 5. Curve 1 in Fig. 5 corresponds to a complete wetting case, whereas curve 2 corresponds to a partial wetting case. Hysteresis occurs when three (in the case of a capillary meniscus) or four (in the case of droplets) intersections of a straight line for pressure P_e (see Fig. 5) with a disjoining/conjoining pressure isotherm are observed, which is only possible for a partial wetting case (isotherm 2 in Fig. 5). Film thicknesses h_β corresponds to a metastable equilibrium thickness, whereas h_u and h_uu correspond to unstable thicknesses; only h_e corresponds to a thermodynamically stable equilibrium thickness of a flat liquid film.[20,21]

It was demonstrated in ref. 20 and 21 that all equilibrium and static advancing/receding contact angles can be calculated using disjoining/conjoining pressure isotherms (see the

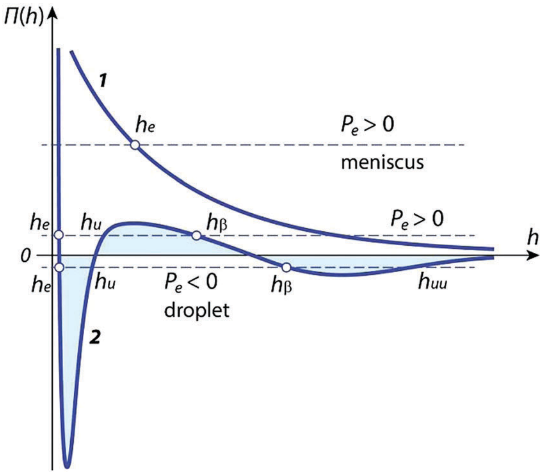

Fig. 5 Schematic presentation of disjoining/conjoining pressure isotherms: (1) complete and (2) partial wetting cases. Here, h_e, h_u, h_uu, and h_β are the thicknesses of stable, unstable, unstable, and metastable wetting films, respectively. Reproduced from ref. 20 with permission from IOPscience, copyright 2009.

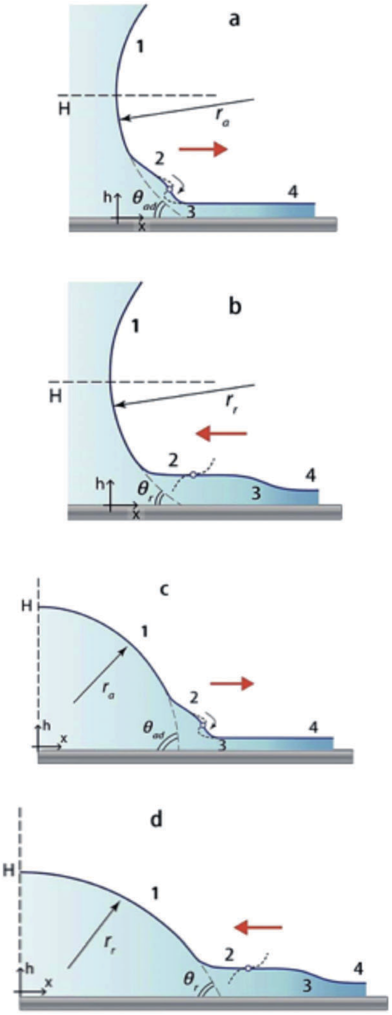

Fig. 6 Transformation of the liquid profile of a capillary meniscus (a and b) and droplet (c and d) under advancing (a and c) and receding (b and d) conditions. (1) Spherical meniscus or droplet; (2) transition zone with a critical marked point (see the explanation in the text); (3) flow zone, and (4) flat film. (a and c) Close to the marked point, the dashed line shows the profile of the transition zone just after the contact angle reaches the critical static advancing value, θ_{ad}, at the beginning of the advancement through a caterpillar motion mechanism. (b and d) Close to the marked point, the dashed line shows the profile of the transition zone just after the contact angle reaches the critical static receding value, θ_r, at the beginning of the sliding motion of a bulk liquid over a thick film.

qualitative explanation of the results presented in ref. 20 and 21) in Fig. 6.

When the pressure in a bulk liquid increases, the interfacial profile of the droplet or meniscus compensates for the excess pressure at the expense of the curvature change, and thus the contact angle also increases. Under these conditions, a macroscopic movement of the liquid profile is not observed; however, the profile moves microscopically. This process can continue over a long period of time if the evaporation/condensation effects are negligible. At the moment a critical value of the liquid pressure or contact angle θ_{ad} is achieved, the meniscus or droplet starts moving macroscopically. If the pressure under the liquid profile is decreased, a similar phenomenon occurs: The profile does not recede until reaching a critical pressure, and the corresponding critical contact angle, θ_r, is achieved. Therefore, within the range of $\theta_r < \theta < \theta_a$, the profile is macroscopically immobile, and only microscopic movement occurs.

If the pressure in a liquid is increased, the profile incline becomes steeper near the critical point[9] in the transition zone (Fig. 6a and c). In the thin film region, flow zone 3 exists where the viscous resistance is very high and the profile moves very slowly. Under a certain pressure, the liquid profile slope reaches a value of $\pi/2$ at the critical point; the flow expands gradually to a thick β-film region, and a fast caterpillar motion begins (Fig. 6a and c).[9]

If the pressure in the bulk liquid is decreased, the slope of the liquid profile in the transition zone within the vicinity of a critical marked point (Fig. 6b and d) becomes more flat. As in the previous case of advancement, a flow zone with high viscous resistance is observed in the thin film region (Fig. 6b and d) where the droplet or meniscus moves very slowly. When the critical pressure is reached, the discontinuous characteristic of the profile should be expected near the critical marked point; however, this profile behaviour is clearly impossible. As a result, profile sliding over a thick β-film is observed.[9] The presence of a thick β-film behind the receding meniscus of an aqueous solution in quartz capillaries was investigated experimentally.[23–25] This experimental fact agrees with conclusions following from the theory of static contact angle hysteresis on a smooth, homogeneous substrate.[9]

In spite of some qualitative experiments confirming this possibility, a precise calculation of all mentioned angles is currently impossible at the current state of science. There is only a limited range of flat liquid films[22] where the disjoining/conjoining pressure can be measured: (i) only within $\Pi(h) > 0$ (under-saturation), and (ii) in flat films satisfying the stability condition, $\Pi'(h) < 0$. For the thickness range of $\Pi(h) < 0$ (which corresponds to an over-saturation), and $\Pi'(h) > 0$ for unstable flat films, there are no currently experimental methods available. Moreover, inside the transition zone (where both capillary and surface forces are equally important) the liquid profile is not flat at all. There have been limited studies taking this into account. Next, the surfaces considered in ref. 20 and 21 are ideal, without roughness, which is frequently not the case in real situations. There has not been a single attempt at considering either the equilibrium or hysteresis contact angles when taking into account the disjoining/conjoining pressure on a rough surface.

2.3. Spread of viscous droplets

The dynamics of the spreading/evaporation process of liquid drops is an important topic of interest because it plays a crucial role in many industrial and material operations. A few such applications, including printing, painting, coating, lubrication, and spraying, have been reviewed.[25] One of the main problems in these applications remains the precise control of all relevant parameters for the droplet spreading/evaporation processes. The substrate temperature and evaporation rate are examples of such parameters that strongly modify the spreading/evaporation dynamics.[26,27]

For viscous spreading of small droplets, the hydrodynamic theory predicts that the initial dynamic wetting is driven by the capillarity and is opposed by the viscous dissipation in the liquid wedge-like region near the contact line. By balancing the capillary and viscous forces, the radius r of the spreading drops (in the case of complete wetting) in scale over time t according to the following power law, which is known as Tanner's law,[28] is $r(t) = R(\gamma t/\mu R)^n$, where $n = 1/10$, R is the drop radius, and μ is the dynamic viscosity. This law can be simply obtained by considering that the shape of the drop is a thin spherical cap, and that the dynamic contact angle θ_D is related to the contact line velocity using the Cox–Voinov relationship[29] of $\theta_D{}^3$ = Ca. Moreover, Tanner's law predicts the long-term spreading, and does not apply for short periods of time.

As the wetting radius of the droplet grows beyond the capillary length (for centimetre-sized drops), gravity becomes the dominant spreading force, and the shape of the drop becomes pancake-like, curved only at the drop rim, yielding a spreading exponent $n = 1/8$ when the bulk phase fluid dissipation dominates, or $n = 1/7$ when the contact line fluid dissipation dominates.[30] A crossover between $n = 1/10$ and 1/8 was reported in experiments conducted by Cazabat and Stuart,[31] whereas Ehrhard[32] found a crossover from 1/10 to 1/7. For liquids with different viscosities, Duvivier *et al.*[33] estimated the coefficient of contact line friction based on the molecular kinetic theory, by fitting the experimental spreading radius $r(t)$ for drops with different viscosities. In their experiment, the authors showed that the contact-line friction of the liquid–air interface *versus* the glass is proportional to the viscosity, and is exponentially dependent on the adhesion. A departure from Tanner's law was reported by de Ruijter *et al.*,[34] and was attributed to a change in the physical mechanism through which the contact line advances across the solid surface. It was also shown that several kinetic regimes associated with different dissipation channels have to be considered, although they have a dominant effect on the kinetics of the wetting process at different time scales. Most studies have focused on understanding the factors (viscosity, density, surface tension, drop volume, and surface wettability) that affect the spreading dynamics of pure liquids. Such studies have been described in the literature based on the hydrodynamic theory.[29,35] However, few experimental or theoretical studies have attempted to investigate the effects of the evaporation rate on the spreading dynamics of a volatile liquid. Ajaev *et al.*[36] found a deviation from Tanner's law when the interface shape changes rapidly in response to rapid changes in the heater temperature. In their work, the evaporation rate was modified by heating the substrate, whereas in our work, we changed the relative humidity, which is one of the easiest parameters to control.

3. Heat and mass transfer

3.1. Evaporation under complete or partial wetting

The spreading/evaporation kinetics is influenced considerably by the presence of contact angle hysteresis in the case of partial wetting. The spreading/evaporation kinetics and spreading/imbibition process of a droplet over a porous surface are remarkably similar. Both processes can be subdivided into three subsequent stages in a partial wetting case (Fig. 7a):[37] stage (1), where a fast spreading of the droplet occurs until its base radius expands, and the contact angle decreases to a static advancing contact angle; stage (2), where a constant radius of the contact line (at its maximum value) occurs while the contact angle decreases from a static advancement to a static receding contact angle; and stage (3), where a shrinkage of the droplet base takes place at a fixed static receding contact angle until a complete disappearance occurs. The main characteristic of partial wetting is the contact angle hysteresis, which results in the occurrence of stage 2, when the droplet edge is pinned. However, no hysteresis appears with complete wetting; therefore, stage 2 of partial wetting is absent in the complete wetting behaviour (Fig. 7b), and there are only two stages of spreading/evaporation or spreading/imbibition over a porous substrate.[37]

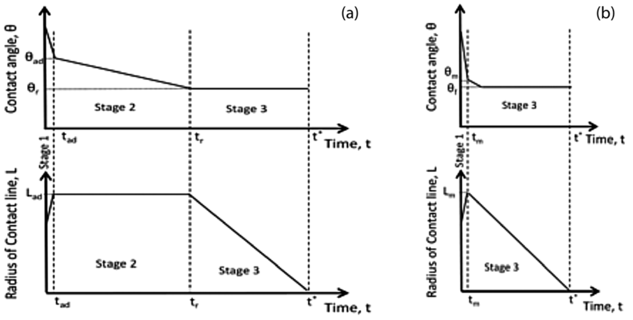

Fig. 7 Simultaneous spreading and evaporation of a droplet (or spreading over a porous surface): (a) partial wetting case: three stages. Here, L_{ad} is the maximum radius of the droplet base, θ_{ad} is the advancing contact angle, t_{ad} is the time when θ_{ad} is reached, θ_{r} is the receding contact angle, t_{r} is the time when θ_{r} is reached, and t^* is the time when the droplet completely disappears (evaporates or penetrates into the porous substrates). (b) Complete wetting case: there are two stages. Here, L_{m} is the maximum value of the droplet base radius, t_{m} is the time when L_{m} is reached, θ_{m} is the contact angle at t_{m}, t^* is the time when the droplet completely disappears, and θ_{f} is the final contact angle at t^*. Note that stage 2 is absent in a complete wetting case.

3.2. Dependence of the evaporation flux on the droplet size

Theoretical and computer simulation studies[37–43] have given the following equation for the evaporation rate of a sessile droplet:

$$\frac{\mathrm{d}V}{\mathrm{d}t} = -\beta F(\theta)L, \tag{10}$$

where, according to,[43]

$$\beta = 2\pi\frac{DM}{\rho}(c(T_{\mathrm{surf}}) - Hc(T_{\infty})), \tag{11}$$

or simply,

$$\frac{\mathrm{d}V(t)}{\mathrm{d}t} = -\alpha L(t), \quad \alpha = \beta F(\theta), \tag{12}$$

where V is the droplet volume; t is time; D, ρ, and M are the vapour diffusivity in the air, density of the liquid, and the molar mass, respectively; H is humidity of the ambient air; and T_{surf} is the average temperature of the droplet–air interface:

$$T_{\mathrm{surf}} = \frac{1}{s}\int_S T_s(s,t)\mathrm{d}s. \tag{13}$$

Here, S is the liquid–air interface, $T_s(s,t)$ is the temperature of the surface at position s on the interface, and T_∞ is the temperature of the ambient air. In addition, $c(T_{\mathrm{surf}})$ and $c(T_\infty)$ are the molar concentrations of saturated vapour at the corresponding temperature, and $F(\theta)$ is a function of contact angle θ, which equals 1 at $\theta = \pi/2$.[38]

Eqn (8) was deduced for the evaporation model, which takes into account only the diffusion of the vapour in the surrounding air. In the case of θ independent of L (the first stage of evaporation), eqn (8) provides an evaporation rate that is directly proportional to the radius of the droplet base, L.

It has been shown[43,44] that the proportionality of the total evaporation flux, J, to the droplet perimeter has nothing to do with the distribution of the local evaporation flux, j, over the droplet surface for sufficiently large droplets (bigger than 1 μm).

Considering the dimensions, it was shown[43,44] that the total flux is $J \sim L$, and that the local flux is $j \sim 1/L$. Note that these properties do not depend on the distribution of the local evaporation flux, j, over the droplet surface. The latter conclusions agree with the previous consideration by Cazabat *et al.*[45] Note that these properties are valid only in the case of diffusion-controlled evaporation, that is, for droplets of greater than 1 μm.

3.3. Thermal phenomena during evaporation

Experiments by David *et al.*[46] showed that the temperature in the bulk of a sessile evaporating droplet substantially depends on the thermal properties of the substrate and the rate of evaporation. Their measurements[46] proved that the temperature of an evaporating droplet is different from the ambient temperature and almost constant in the course of the evaporation. In ref. 47, the dependence of the total vapour flux, J, on the radius of the droplet base, L, and the contact angle, θ, was investigated using numerical simulations. All calculations were performed with effects of both the local heat of vaporisation (LHV) and the Marangoni convection (MC) included. The results were obtained for substrates made of materials with various thermal conductivities, and compared to those calculated for the isothermal cases by Hu and Larson[44] and Schonfeld *et al.*[48] In the case of a highly heat-conductive solid support (copper), the difference between the present simulations and the results from ref. 44 and 48 for an isothermal case do not exceed 3%.[47] The latter is because of a small temperature change at the droplet surface, which is close to the isothermal conditions. However, if other materials are used with lower heat conductivity (down to the heat conductivity of air), then the evaporation flux is substantially reduced as compared with the isothermal case.[47] Such a flux reduction is connected to the noticeable temperature decrease of the droplet surface.

In ref. 47, the mean temperature of the droplet surface T_{surf} (eqn (13)) was introduced, where S is the surface area of the evaporating droplet. The dimensionless total flux $J/J_{\pi/2}(L,T_{\mathrm{surf}})$ was plotted in ref. 47, where $J_{\pi/2}$ is the total flux when the contact angle is equal to π/2. All calculated total fluxes[47] for all substrates decrease to a single universal dependence of the total vapour flux, J, *versus* contact angle, θ. This universal dependency coincides with the dependency for the isothermal case if T_{surf} is used as the temperature of the droplet–air interface. The latter shows that the variation in surface temperature is the major phenomenon influencing the evaporation rate (Fig. 8 and 9). Note that $J_{\pi/2}$ in Fig. 8 was calculated by taking the temperature of the droplet surface as equal to the temperature of the substrate, $T_{\mathrm{substr}} = T_\infty + 5$ K, whereas in Fig. 9 the average temperature, T_{surf}, was used instead.

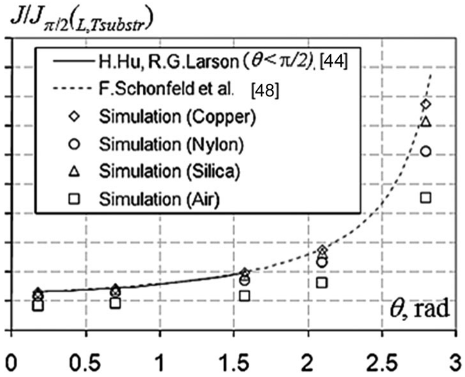

Fig. 8 Rescaled dependence of the total vapour flux from the droplet surface, J, on contact angle θ, where L = 1 mm. Both the latent heat of vaporisation and the Marangoni convection were taken into account. Reproduced from ref. 47 with permission from Elsevier, copyright 2007.

The heat and mass transfer at a droplet impinging on a hot wall were investigated experimentally and numerically.[49] These experiments were conducted using refrigerant FC-72 within a saturated vapour atmosphere. The droplet dynamics and heater temperature very close to the solid–fluid interface were captured using high spatial and temporal resolutions. The boundary conditions for the numerical simulations were chosen according to the experiments. The simulations accounted for

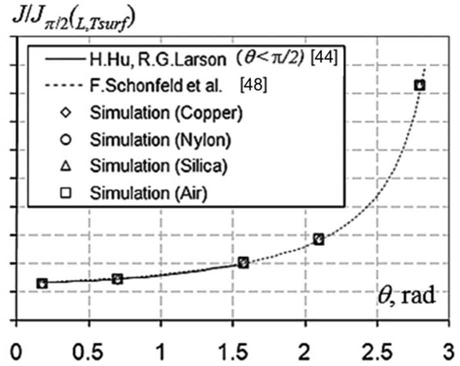

Fig. 9 Universal behaviour: rescaled dependence of the total vapour flux from the droplet surface, J, on the contact angle θ, where L = 1 mm. Both LHV and MC are taken into account. All points from Fig. 5 are on the universal isothermal curve (similar to Fig. 8), and are indistinguishable, when T_{surf} is used as the temperature of the droplet–air interface. Reproduced from ref. 47 with permission from Elsevier, copyright 2007.

the complex two-phase flow including the evaporative mass transfer. Special attention was given to the local heat and mass transfer close to the moving three-phase contact line. The numerical and experimental results were compared to give insight into the basic heat transport mechanisms occurring during a drop impact, and to quantify their relevance for the overall heat transfer. It turns out that the convective heat transfer is dominant during the initial stage of the impact corresponding to the droplet spreading, whereas at the final stage of impact, corresponding to evaporation of a sessile droplet, a considerable part of the total heat transfer occurs within the direct vicinity of the three-phase contact line. The heat transfer during a single droplet impingement onto a hot wall has also been analysed.[49] The developed numerical model also accounts for the thermal effects occurring at the moving three-phase contact line. The results of the numerical calculations were compared with the experiments, and were found to be in good agreement. The heat transfer performance was found to be substantially different during the different phases of the drop impingement process. The wall heat transfer was observed to be the strongest during the spreading phase, whereas the evaporation took place mainly during the receding phase. These observations can be attributed to a change in flow pattern within the droplet during the different phases. A strong local heat transfer near the three-phase contact line has been observed in all stages of impact, but is particularly important when the droplet approaches the sessile situation. The effects of the Reynolds number on the heat transfer and evaporation have been investigated systematically using a numerical model. In the future, the authors[49] plan to use larger variations to identify the influence of other parameters such as the Weber number or wall superheat.

When using various models of new energy-saving dishwashers, one annoying aspect occurs: plastic dishes remain wet after the drying cycle, whereas ceramic dishes or metal cutlery are quite dry. To begin understanding the different drying behaviours of different materials, sessile drop evaporation experiments on substrates with dissimilar thermal conductivities have been conducted.[50] A total of 30 evaporation experiments on pure water drops of different sizes were conducted and analysed.[50] It was found that the thermal properties of a substrate have a strong influence on the evaporation time of a sessile droplet. A numerical model describing the transient heat conduction in both the drop and substrate, as well as the vapour diffusion in the gas, was developed, and the numerical predictions of the drop evolution show a good agreement with the experimental data.[50]

The effects of the thermal properties of the substrates on the overall evaporation time of water drops placed on them were investigated.[50] Glass and silicon substrates were used, upon which a grafted layer of polystyrene was deposited to ensure the same wettability; the heat capacities of both materials were demonstrated to be very similar. It was concluded from the experiments that the higher thermal conductivity of silicon accelerates the drop evaporation by more than 10%. A numerical model describing the transient heat conduction in a droplet and substrate, as well as vapour diffusion in the gas, was developed. It was shown that the transient heat transport governs the evolution of the local temperature distribution at the liquid–gas interface, and therefore the evaporation rate. The numerical simulations agree well with the experimental results of the evaporation rate.[50]

In ref. 51, experimental and theoretical investigations of a water drop impacting an electrospun polymer nanofibre mat deposited on a heated stainless-steel foil were conducted. The measurements encompass the water spreading over and inside the mat, as well as the corresponding thermal field. The results indicate that the presence of polymer nanofibre mats prevents a receding motion of the drops after their complete spreading, and promotes the moisture spreading inside the mat over a large area of the heater, which facilitates a tenfold enhancement of the heat removal as the latent heat during drop evaporation. Drop spreading after impact on a polymer nanofibre mat is almost instantaneously followed by water penetration into the pores, after which heat is removed from the underlying hot stainless-steel foil, corresponding to the latent heat of water evaporation in direct contact with the foil.[51] At the first stage of cooling, the heat flux is on the order of up to 0.3 kW cm^{-2}, which is a general characteristic of spray cooling. During the second stage, heat is removed through conduction along the foil toward the cold central spot, which appears at stage 1, and only then is used for water evaporation. The drop imbibition and evaporation introduce a limiting stage that prolongs the drop evaporation process to several tens of seconds, and diminishes the overall heat flux. It is expected that the limiting stage can be significantly shortened with highly conductive metal nanofibres instead of the polymer nanofibres used in ref. 51.

3.4. Modelling of convective transport

The vapour distribution around a sessile droplet was recently studied using experimental[52] and numerical[53,54] approaches for purely diffusive evaporation. Kelly-Zion *et al.*[52] have recently shown using infrared spectroscopy and computed tomography that the vapour emitted by sessile drops at room temperature behaves differently compared to the commonly accepted diffusion-limited model. Models taking into account convection have been developed to predict the evaporation time and obtain the best reagent concentration for combustion.[55–57] The most commonly used model, the Spalding evaporation model, takes into account convection using the calculation of mass and heat balance separately during each phase at the interface.[58] This model is based on numerous assumptions (an isothermal spherical droplet, a quasi-steady gas boundary, vapour–liquid phase equilibrium at the interface, the air and vapour behaving like a perfect gas, and the use of Fick's law of diffusion) that are similar to the purely diffusive model used in this study. This model, based on the Spalding mass number, slightly over predicts the evaporation rate of droplets evaporating under reduced gravity conditions *i.e.*, for purely diffusive evaporation.[70] For this reason, a purely diffusive model has been chosen as the basis of our empirical model.

New models that are able to correctly predict diffusive and convective evaporation are emerging,[59,69] although their use has been limited to peculiar fluids. Therefore, the aim of this article is to determine the limits of purely diffusive models and to develop, based on numerous experiments, an empirical model that accurately describes the evaporation rate of a sessile droplet on a heated substrate, regardless of the temperature or type of fluid. The atmospheric contribution to sessile droplet evaporation will also be investigated numerically.

3.5. Simultaneous spreading and evaporation in the case of complete wetting

In the case of complete wetting, the droplets spread out completely over a solid substrate, and the contact angle decreases to zero. Lee *et al.*[60] considered the process of simultaneous spreading and evaporation of sessile droplets in the case of complete wetting. To model the spreading, they considered Stokes equations under a low slope approximation.[60] The total evaporation flux, J, was used according to eqn (10). The entire process of spreading/evaporation was divided into two stages: (i) an initial short but fast spreading stage, when the evaporation can be neglected, and the droplet volume, V, is approximately constant; and (ii) a second (stage 3 in Fig. 7) slower stage, when the spreading process is almost over, the contact angle is approximately constant, and the evolution is determined mostly based on the evaporation.

In the case of complete wetting, the contact angles are sufficiently small (less than 20°), and function $F(\theta)$[38] varies from 0.64 to 0.68. That is, according to the previous study, α can be considered a constant with a good degree of approximation.

Solution of the deduced system of equations in non-dimensional form gives a universal law of the process of simultaneous spreading and evaporation for the case of complete wetting, which is confirmed through experimental data from various sources[60] (Fig. 10 and 11).

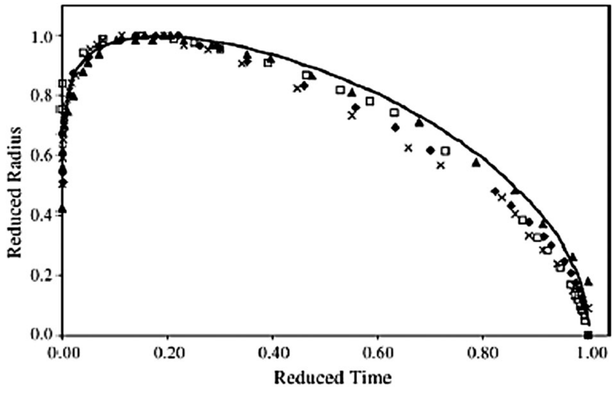

Fig. 10 Dependency of a reduced radius of the droplet base, L/L_0, against reduced time, t/τ_0, calculated according to ref. 34 for a comparison of different liquids spreading/evaporating on a solid substrate. Experimental data extracted from various sources:[34] ♦ octane; ☐ water; ▲ silicon Oil (3 μL); × silicon oil (0.5 μL); and theoretical prediction. Reproduced from ref. 60 with permission from Elsevier, copyright 2011.

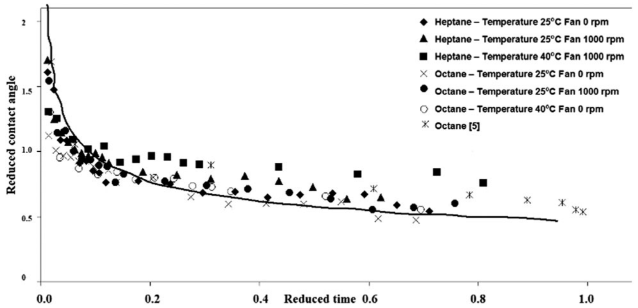

Fig. 11 A reduced contact angle θ/θ_m, where θ_m is the contact angle when the droplet base radius reaches the maximum value, against reduced time t/τ_0 calculated according to the theory presented in ref. 60 and experimental data from various sources. Reproduced from ref. 60 with permission from Elsevier, copyright 2011.

3.6. Simultaneous spreading and evaporation in the case of partial wetting

As we mentioned above for the case of partial wetting, the contact angle hysteresis is the most important feature: in the presence of contact angle hysteresis, the evaporation of a sessile droplet in a non-saturated vapour atmosphere goes through four consequent stages (Fig. 7a). Only the two longest stages, 2 and 3, are considered below, and are referred to as stages I and II.

A detailed study of stages I and II for a pure liquid was previous conducted in ref. 61, where it was assumed that during both stages of evaporation the droplet retains a spherical shape. During both stages of evaporation, the mass conservation law has the form given by eqn (8), where parameter β does not depend on the age of the droplet, as described in ref. 61, and hence remains constant. The methods for calculating parameter β, provided in ref. 61, are as follows:

- The first stage of evaporation (stage 2 in Fig. 7a): during this stage of evaporation, the radius of the contact line remains constant and is equal to L_{ad} (Fig. 7a). The equation deduced in ref. 61 represents a unique curve describing the first stage of evaporation. A comparison of the presented theory with the available experimental data from various sources is presented in Fig. 12, and shows a very good agreement between the theory prediction and experimental data.
- The second stage of evaporation (stage 3 in Fig. 7a): during this stage, the contact angle remains constant but the radius of the contact line decreases. The equation deduced in ref. 61 represents a unique curve describing the second stage of evaporation (Fig. 13).

3.7. Evaporation of micro-droplets of pure liquids

For all previous considerations, only a diffusion model of evaporation was taken into account: the kinetic effects at the liquid–gas interface (Hertz–Knudsen–Langmuir equation), the dependency of the vapour pressure on the droplet curvature, and the Stefan flow were all neglected. It was shown in ref. 62 and 63 that the influences of these phenomena are negligible if the size of an aqueous droplet is bigger than 1 μm. However, for smaller droplets, these phenomena become important.

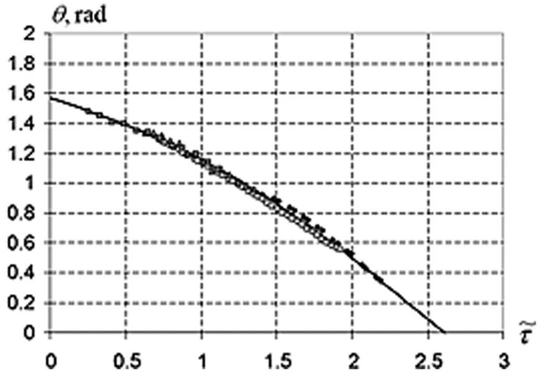

Fig. 12 First stage of evaporation according to equation in ref. 61. Dependence of contact angle, θ, on dimensionless time, $\tilde{\tau}$.[61] Experimental point from various literature sources. Reproduced from ref. 61 with permission from Elsevier, copyright 2008.

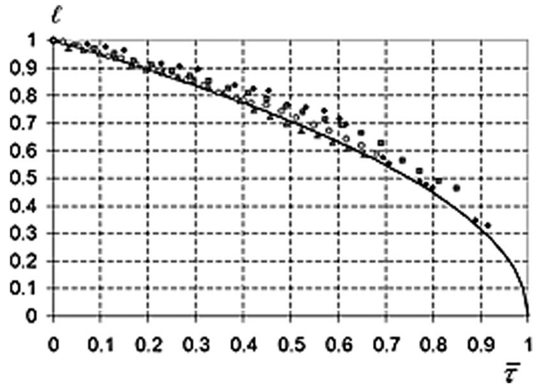

Fig. 13 Second stage of evaporation. Dependence of dimensionless radius of the contact line, ℓ, on dimensionless time, $\bar{\tau}$.[61] Experimental point from various literature sources. Reproduced from ref. 61 with permission from Elsevier, copyright 2008.

Computer simulations of the evaporation of small sessile water droplets were conducted in ref. 62 and 63. The adopted model[62,63] combines diffusive and extra models of evaporation, as mentioned above. The effects of latent heat of vaporisation, thermal Marangoni convection, and Stefan flow in the surrounding gas were also taken into account. The investigated system was an aqueous droplet on a heat conductive substrate (copper) in air.[62,63] The modelling results allowed estimating the characteristic droplet sizes when each of the above mentioned phenomena become important or can be neglected. Note that ref. 62 and 63 were the first papers focusing on this area, and only a qualitative, and not quantitative, influence of the droplet size on evaporation was considered. That is, a number of extra phenomena, for example, non-uniformity of the mass accommodation coefficient, were not considered.

The model used in ref. 62 and 63 is valid only for a droplet size of larger than the radius of the surface forces, which is around 10^{-7} m = 0.1 μm. That is, the data presented in ref. 62 and 63 for a droplet size of smaller than 10^{-7} m are used only to show the specific trend. The results obtained in ref. 62 and 63 can be summarised as follows (Fig. 14): (i) deviation of the saturated vapour pressure caused by the droplet curvature (Kelvin's equation) can be neglected when the radius of the droplet base, L, is larger than 10^{-7} m, (ii) a deviation from the pure diffusion model of evaporation can be neglected for a droplet size of bigger than 10^{-6} m, and deviations from the diffusion model become noticeable only if the droplet size is less than 10^{-6} m. These deviations are caused by an increasing influence of the kinetic effects at the liquid–gas interface (Hertz–Knudsen–Langmuir equation), and this theory should be applied along with the diffusion equation of vapour in air if the droplet size is less than 10^{-6} m.

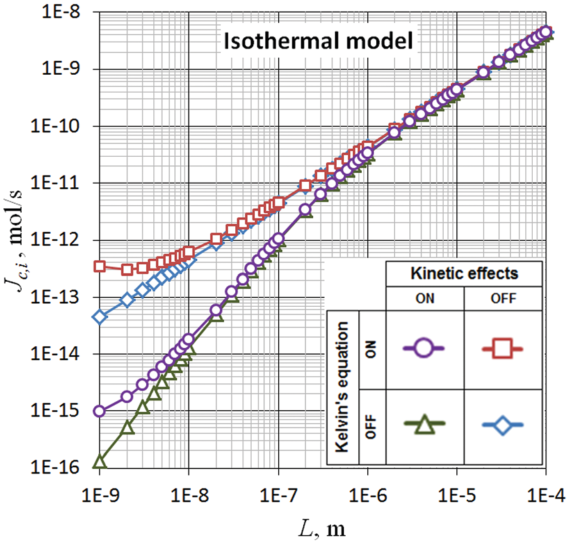

Fig. 14 Dependence of total molar evaporation flux, $J_{c,i}$, on aqueous droplet size, L, for isothermal model of evaporation. The parameters used are θ = 90°, and a relative air humidity of 70%. Note: the results for $L < 10^{-7}$ m do not have any physical meaning because additional surface forces must be included in the model. These points are shown to demonstrate the trends of the curves, which were redrawn from ref. 63. Reproduced from ref. 63 with permission from Springer, copyright 2011.

The latter conclusions show that a consideration of the evaporation of microdroplets with a size of less than 10^{-7} m in terms of both the deviation of the saturated vapour pressure caused by the droplet curvature and the kinetic effects should be included.

The latent heat of vaporisation results in a temperature decrease at the surface of the droplet. For this reason, the evaporation rate is reduced. This effect is more pronounced in the case of diffusion-limited evaporation ($L > 10^{-5}$ m), when the vapour pressure at the droplet surface is saturated and determined by the local temperature. The effect of Marangoni convection in aqueous droplets is negligible for droplets of size $L < 10^{-5}$ m. For the system considered above, the Stefan flow effect appeared to be weaker than the effect of thermal Marangoni convection for $L > 10^{-4}$ m, but stronger for $L < 10^{-4}$ m. However, in all cases, its influence is small and can be neglected. The model presented in ref. 38 and 39 can be applied for evaporation of any other pure simple liquid, and not aqueous droplets only.

According to the model of diffusion for limited evaporation, the evaporation flux, $J_{c,i}$, must be linearly proportional to the

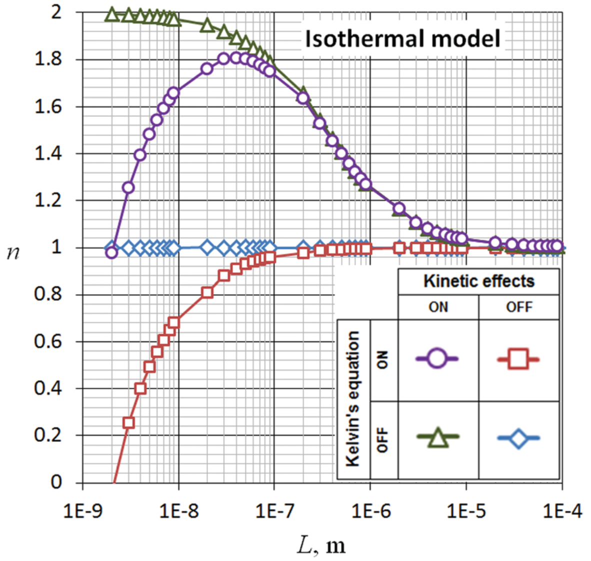

Fig. 15 Exponent n for the dependence $J_{c,i} \sim A(\theta)\cdot L^n$ for the isothermal model of evaporation. The parameters used are $\theta = 90^\circ$, and relative air humidity of 70%. Note that results for $L < 10^{-7}$ m do not have physical meaning because surface forces must be included in the model here. These points are shown to demonstrate the trends of the curves, which were redrawn from ref. 63. Reproduced from ref. 63 with permission from Springer, copyright 2011.

droplet size, L, that is, $J_{c,i} \sim L$. The latter is in agreement with the data presented in Fig. 14 for droplets larger than 10^{-6} m. However, for a pure kinetic model of evaporation (no vapour diffusion or uniform vapour pressure in the gas), flux $J_{c,i}$ is supposed to be proportional to the area of the droplet's surface, that is, in the case of pinned droplets (constant contact area) $J_{c,i} \sim L^2$ should be satisfied. To check the validity of the latter models for various droplet sizes, it was assumed in ref. 62 and 63 that the dependency of the evaporation flux on the droplet radius has the following form: $J_{c,i} \sim A(\theta)\cdot L^n$, where n is the exponent to be extracted from the computer simulation results,[62,63] and A is a function of the contact angle, θ.

The calculated values of n are presented in Fig. 15. This figure shows that exponent n, as expected, is equal to 1 for a pure diffusive isothermal model of evaporation within the whole studied range of L values (diamonds in Fig. 15). Fig. 15 shows that the diffusion model of evaporation dominates for droplets with a size of larger than 10^{-5} m, that is, for droplets bigger than 10 μm when both the effects of the kinetics and Kelvin's equation are taken into account along with pure diffusion.

Considering only the kinetic effects along with the diffusion, and ignoring the Kelvin equation (triangles in Fig. 15), results in a smooth transition from linear dependence $J_{c,i} \sim L$, that is, $n = 1$ (diffusive model), to quadratic dependence $J_{c,i} \sim L^2$, that is, $n = 2$ (kinetic model), as the size of the droplet decreases to $L = 10^{-9}$ m (see Fig. 15). The latter indicates that $J_{c,i}$ tends to be proportional to L^2 as the size of the droplet decreases, which means that the evaporation flux becomes proportional to the area of the liquid–gas interface. However, the influence of the curvature (Kelvin's equation) on the saturated vapour pressure results in a substantially lower exponent n as compared with kinetic theory (Fig. 15). Note that the latter occurs only for a droplet completely within the range of surface forces, that is, less than 10^{-7} m.[9] Below this limit, the droplet no longer has a spherical cap shape even on the top (micro-droplets according to ref. 9). The evaporation process in the latter case should be substantially different from that considered above. Thus, the range of sizes of less than 10^{-7} m is not covered by the presented theory.

4. Flow instabilities

Patterns related to the flow structure in a sessile droplet and its surrounding air–vapour environment may reveal the leading mechanisms driving the various instabilities observed and explain the dynamical regimes that take place in the course of evaporation. Therefore, this chapter presents some state-of-the-art methods and algorithms that can help us better understand the various flow instabilities observed in the evaporation of sessile droplets. Although it is clearly a transient phenomenon, we use for the first time a frozen-time technique associated with a one-sided model to study the flow structure sensitivity of the evaporation rate in order to study its related bifurcation diagram. Then, a two-sided and unsteady model is used to investigate highly nonlinear regimes associated with high evaporation rates. The approaches we followed in this study are first presented, and the results and their limits obtained are then discussed. It turns out that physically refined models can be used to reproduce and investigate most of the triggering mechanisms of the flow instabilities that take place during the evaporation process of a sessile droplet.

The effects of fluid flows that develop during the evaporation process of a sessile droplet deposited on a substrate were investigated because they play an important role in the related dynamics of the entire evaporation process. At least three main mechanisms drive the fluid flow in this process under earth conditions: (i) drainage in the droplet, (ii) buoyancy during the liquid and vapour phases, and (iii) thermo-capillary forces, which may induce a fluid flow in the liquid or vapour phase, or in both phases. Owing to its spherical-cap shape, the evaporation rate in a sessile droplet deposited on a heated substrate is predominant within the vicinity of its contact line for contact angles of lower than 90. This induces drainage from the droplet centre toward its periphery, resulting in a radial flow (Stefan flow) as long as the contact line is pinned to the substrate.[64–67] Outside the droplet, vapour diffusion toward the surrounding air unavoidably induces gradients in the vapour concentration, which under gravity conditions results in solutal buoyancy in the vapour phase. Moreover, because evaporation is in essence an endothermic process, thermal gradients also appear in both the liquid and vapour phases, and thus thermal buoyancy also takes place in both fluid phases. Finally, thermal gradients, and most likely solutal gradients (for binary and multicomponent liquids), appear along the liquid–vapour interface, inducing surface-tension gradients that can drive the flow

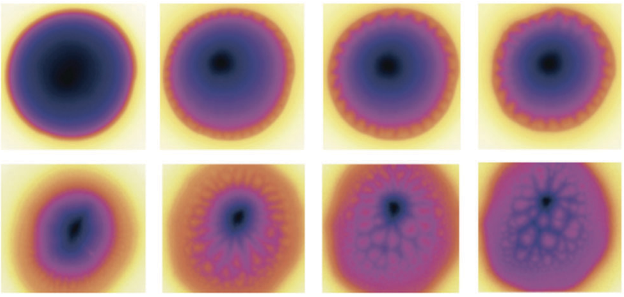

Fig. 16 Infrared images (top views) of two evaporating sessile droplets deposited on a heated substrate at four times during the evaporation process. Upper row, ethanol droplet (initial radius of 52.2 mm, substrate temperature T_s = 46 °C); lower row, FC-72 droplet (initial radius of 53.8 mm, substrate temperature T_s = 51 °C). The images were taken every 100 ms. Reproduced from ref. 77. Reproduced from ref. 77 with permission from Elsevier, copyright 2011.

in both phases and become the prevailing driving mechanism under micro-gravity conditions.

Therefore, the dynamics of an evaporating sessile drop result from the competition between these three driving mechanisms, whose ratio continuously evolves in the course of the droplet evaporation process as the geometry accordingly changes. For droplet diameters of up to a few millimetres, the thermo-capillary force commonly dominates the buoyancy (Bd $\ll$ 1), and the resulting thermo-convective flow is at least one order of magnitude greater than that resulting from drainage alone (Stefan flow). Moreover, the flow structure is also very different in these two cases: it is organized into torus roll(s) in the former case, and is a purely radial flow in the latter.[66,67] Furthermore, at high evaporation rates, this thermo-convective torus fluid flow is prone to instability, and fully three-dimensional structures appear and can form hydrothermal waves.[68,77,79,80] Fig. 16 shows infrared snapshots taken from above at four moments of evaporation (at 10% increments of the total evaporation time, starting from the beginning on the left) for ethanol (upper row) and FC-72 (lower row) droplets deposited on a heated substrate.

These snapshots show that complex dynamical flow structures develop in a very different way, depending on the evaporation conditions. For the case of ethanol (Fig. 16, upper row), the fluid flow seems to develop first as a torus roll located close to the outer ring of the droplet, and this torus is then destabilized into cells, whose azimuthal wavelength decreases with time. For the case of FC-72 (Fig. 16, lower row), which evaporates at a much higher rate than ethanol because it is a much more volatile liquid in air, the outer torus roll seems to persist for a while, and a chaotic cell pattern meanwhile develops from the very early evaporation times and invades the whole central part of the liquid droplet.

In addition to several very convincing sessile droplet experiments, which display quite complex instability routes, linear and nonlinear stability analyses of the evaporating plane of liquid layers have recently been undertaken.[82,83] However, the authors used a different flow structure of the base state resulting from geometrically different configurations. That is, we selected a different way to investigate the stability problem of thermo-convective flows that take place during the evaporation process of a sessile droplet, as described below. It is also necessary to take into account both the time-dependent evolution of the spherical-cap shape of the liquid–vapour interface and the dynamics of the contact line, which are still unobtainable from most off-the-shelf numerical models and consequently have yet to be solved to the best of our knowledge. Thus, alternate directions and simpler configurations can be considered for a better understanding of the flow stability of a sessile droplet.

4.1. Relevance of frozen-time approaches

The evaporation process of a sessile droplet is clearly a transient phenomenon, and usually displays three main stages from a purely geometrical point of view (Fig. 7a). In the first stage, the contact line is pinned to the substrate at a constant droplet diameter, and evaporation proceeds with a decreasing contact angle, up to the lower limit. When reaching this limit, the second evaporation stage takes place with a receding contact line at an approximately constant contact angle, resulting in a decreasing droplet diameter. Finally, the third stage occurs when the droplet loses its spherical-cap shape and evolves into a very thin film as it enters the microscopic scale.

Fortunately, as indicated through experimental observations (Fig. 16), most of the flow instabilities arise during the first stage, whereas evaporation proceeds at a constant droplet diameter and decreasing contact angle. It is also clear that in this first stage the rate of change of the contact angle with respect to time is much smaller than the rate of change of any thermal or fluid-flow perturbations, and thus a quasi-steady-state can be assumed throughout the first stage for the purposes of a stability analysis. Moreover, for low evaporation rates, the evaporating process of a sessile droplet is often controlled based on the vapour diffusion in the surrounding air outside the droplet.[84] With these cases, the duration of this first evaporation stage is much longer than the vapour diffusion time, and thus here again a quasi steady-state can be assumed in this stage, and a one-sided model can also be relevant.[82] This is one of the simplest representative models, and has therefore been used in most of the present work, and is introduced below.

The simplifying assumptions we have made to derive the physical model related to the one-sided frozen-time model are as follows (Fig. 17). Only the substrate and liquid drop are considered, and the

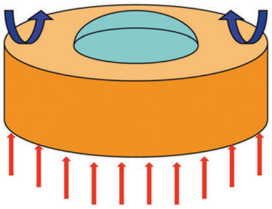

Fig. 17 Sketch of one-sided frozen-time evaporation model of a sessile drop deposited on a heated substrate. Reproduced from ref. 109 with permission from Elsevier, copyright 2015.

droplet geometry is fixed (pinned contact line and constant contact angle). Heat transfer across the liquid–vapour interface is accounted for in the energy balance throughout the global heat transfer coefficient, which includes a linearized liquid–vapour phase change considering a uniform and constant vapour concentration gradient in the surrounding droplet environment.[82] All thermo-physical properties are assumed to be constant, taken at room temperature, and the lower wall of the substrate is heated at a constant heat flux.

4.2. Parametric study using one-sided steady-state model

For a better understanding of the various instability mechanisms that take place during the evaporation process of a sessile droplet, we first investigated the influence of the evaporation rate on the pattern selection for several dynamic Bond numbers (Bd = Ra/Ma, where Ra and Ma are defined in eqn (14) and (15)), that is, various ratios of the driving mechanisms.

$$\mathrm{Ra} = \frac{g\beta}{\nu\alpha}(T_{\mathrm{S}} - T_{\infty})L_{\mathrm{C}}{}^{3}, \tag{14}$$

$$\mathrm{Ma} = -\frac{\mathrm{d}\gamma}{\mathrm{d}T}\frac{L\Delta T}{\mu\alpha}, \tag{15}$$

where g is the gravitational acceleration, β is the volumetric expansion coefficient, ν is the kinematic viscosity, α is the thermal diffusivity, g is the surface tension, μ is the dynamic viscosity, and L_{C} is the characteristic length.

Keeping in mind that the frozen-time approach can only be representative of a low evaporation rate in which the dynamics are low with respect to the time duration of the first evaporation stage, it is nevertheless noteworthy that symmetrical breaks already occur in such simple cases. As an illustration, Fig. 18 and 19 show bifurcation diagrams for Bd = 1 and 1/1.75, respectively, and Pr = 6, plotting in dimensionless variables the mean droplet velocity, V_{mean}, *versus* the applied heat flux at the substrate lower wall, λ. In these two figures, the inserts represent top views of the isotherms and velocity field over a droplet-free surface, along with isotherms, streamlines, and velocity vectors in radial or diametric cross sections. Starting the continuation from the origin (isothermal motionless droplet in a saturated environment) in both cases, we first proceed along the fundamental branch. In Fig. 18 (Bd = 1), its slope increases slowly at first and then rises much more steeply. It then intersects two secondary branches, and thus two bifurcations occur in this diagram. The fundamental branch is characterized by the axisymmetric mode, which displays concentric circular isotherms in the top view, whereas the cross section reveals that the liquid flow structure is made up of two concentric torus rolls. It is noteworthy that these rolls rotate in the same direction (upward along the free surface) because they are predominantly oriented based on the Marangoni force for the considered values of the dynamic Bond number. Therefore, in this fluid flow configuration, the higher the fluid flow velocity, the higher the shear stress in between the co-rotating rolls, and thus instability is very likely to occur and indeed does so as expected. Fully three-dimensional fluid flow structures appear along the two bifurcated branches, which exist for relatively high evaporation rates, as shown in the experiments. The two concentric torus roll structures are replaced by a ring roll in which the fluid flow organizes itself into asymmetric donut-like structures to reduce the shear stress.

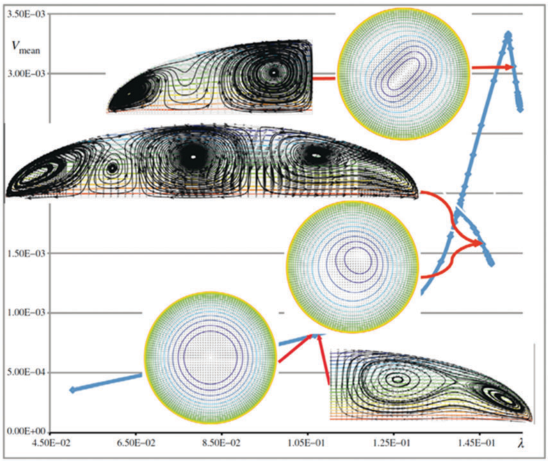

Fig. 18 Bifurcation diagram of the one-sided frozen-time evaporation model of a sessile drop deposited on a heated substrate for Bd = Ra/Ma = 1. Reproduced from ref. 109 with permission from Elsevier, copyright 2015.

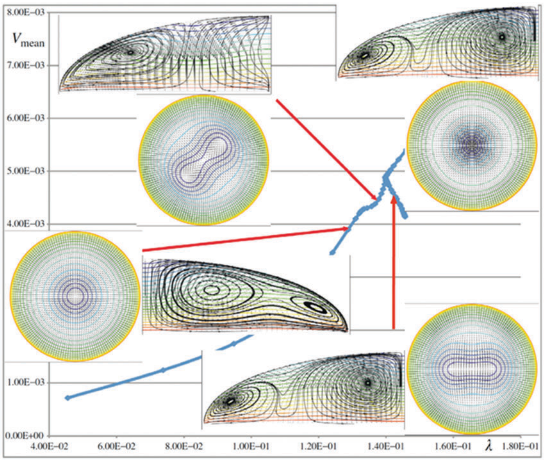

Fig. 19 Bifurcation diagram of the one-sided frozen-time evaporation model of a sessile drop deposited on a heated substrate for Bd = Ra/Ma = 1/1.75. Reproduced from ref. 109 with permission from Elsevier, copyright 2015.

Fig. 19 shows a comparable behaviour for Bd = 1/1.75, despite the fact that the flow structure along the bifurcated branches are slightly different than at Bd = 1, owing to the stronger influence of the Marangoni force with respect to buoyancy. In this case, after the first bifurcation of the fundamental branch, two cells appear inside the outer torus, which gather in the bifurcated branch.

Furthermore, it turns out from this parametric study that as Bd diminishes, the cellular convection overcomes the torus-like convection within the droplet core region. In addition, the droplet geometry (wetting angle, and its spherical-cap aspect ratio) determines the fluid flow pattern (number of structures). Finally, all asymmetric fluid flow structures encountered on the bifurcated branches are unstable, and thus a transient solution should occur toward either a stable state or an unsteady regime.

The one-sided model allows a one-way coupling between the liquid and gas phases in which a linear behaviour is assumed in the gas phase around an *a priori* prescribed base state of both the heat and mass transfers along with the phase change itself. Therefore, only nonlinearities that are accounted for arise during the liquid phase. Despite this quite restrictive assumption, the outcome of the one-sided parametric study is that three-dimensional instabilities can be triggered in the droplet. However, one may wonder whether the instabilities arising from the gas phase would have greater instability than those coming from the liquid phase, or if the actual interactions between the liquid and gas phases might not in turn be more destabilizing. We now address this problem by considering a two-sided model, which is clearly more suitable to correctly account for a fluid flow and heat and mass transfers in the surrounding air and vapour phases. This enables us to investigate highly nonlinear regimes, whereas a full two-way coupling is now accounted for. Moreover, because the dynamics of an unstable regime exhibit much shorter time-scales than the total evaporation time, an unsteady approach is also required. Therefore, to address such computations with affordable computational resources and restrained elapsed times, we considered an axisymmetric two-dimensional two-sided model, which is presented in the following section.

4.3. Two-sided model to investigate highly nonlinear regimes

Herein, we present two-sided numerical models of evaporating ethanol drops on heated substrates. These models are based on real experimental studies[79,81] and take into account heat and mass transfers in both liquid and gaseous adjacent phases. The first model uses a steady state formulation of the problem equations as evaporation occurs into the ambient atmosphere, and can be considered as a steady-state process. The second model uses an unsteady approach as evaporation occurs in a closed chamber, and only the first 20 s of the process are available experimentally (parabolic flight experiment). Two-sided models allow us to predict the vapour transfer from the droplet surface into the ambient atmosphere or into a closed chamber, and to determine the vapour flux distribution along the droplet surface, which results in physically correct (corresponding to actual experiments) interfacial conditions at the droplet surface.

Because the droplet evaporation during the experiments proceeds into the ambient atmosphere or into a chamber with a size much bigger than that of the droplet, the gaseous phase is usually modelled as a semi-infinite medium; the computational domain, however, cannot be infinite and must be bounded either by the chamber walls or by an artificial boundary. Therefore, for the problem of vapour diffusion into an unbounded ambient atmosphere, the size of the computational domain is chosen to be 100 times larger than the size of a droplet, which results in an evaporation rate error (owing to the presence of the outer boundary) of less than 1%, as compared to the rate of droplet evaporation into a semi-infinite medium. In addition to the droplet and vapour phases, a heat conducting solid substrate is included in the models.

Thus, owing to the presence of a gaseous phase, the computational domain in the two-sided models is much bigger than in the equivalent one-sided models. Therefore, one of the assumptions made is the axial symmetry of the model, which reduces the dimensions of the problem down to two independent spatial coordinates (radial and vertical) and substantially speeds up the computational process as compared to a fully 3D model. The origin of the cylindrical system of coordinates is located in the plane of the substrate–droplet interface, and the z-axis coincides with the axis of the droplet's symmetry.

The material parameters in the models are drawn from the experimental parameters. The temperature difference between the heated substrate and the ambient environment is chosen to be 15 $^\circ$C, similar to the particular experiments. Because the temperature change mostly occurs in the air domain (the medium with the lowest heat conductivity in the system), its dynamic viscosity, heat conductivity, and vapour diffusivity were taken as functions of local temperature.

Because the flow velocities in the atmosphere and droplet are much lower than the speed of sound, the air and liquid are modelled as incompressible Newtonian fluids (Navier–Stokes equations). The boundary conditions at the droplet surface for the Navier–Stokes equations include the balance of normal (Laplace pressure) and tangential (thermos-capillary forces) components of the full stress tensor, as well as the continuity of the tangential component of the velocity (no-slip condition) and discontinuity of the normal component of the velocity owing to the evaporation process (Stefan flow). The no-slip boundary condition was applied on all solid surfaces. In the case of evaporation into a semi-infinite medium, at the outer (artificial) boundary of the gaseous domain, the conditions of the zero normal stress (open boundary), ambient temperature, and ambient vapour concentration (zero for ethanol vapour) were applied.

The vapour diffusion–convection equation with a temperature-dependent diffusion coefficient was solved in the air domain using the boundary condition of saturated vapour concentration at the droplet surface, which in turn was also considered as a function of the local droplet temperature (Clausius–Clapeyron equation). No penetration boundary condition was applied for this equation at the solid walls.

The equation of conductive heat transfer was solved in the solid domain, with conductive and convective heat transfers in the fluid domains (liquid and air) under boundary conditions of a constant heater temperature underneath the substrate, and constant ambient temperature at the outer boundaries. At the liquid–air interface, a heat sink owing to evaporative cooling (latent heat of vaporisation) was applied as a function of the local evaporation rate.

A Boussinesq approximation was used to account for the buoyancy in both the liquid and air domains. These forces were calculated based on the dependence of ethanol and air density on the temperature, and of the air density on the vapour concentration. Integration of the local evaporation rate along the droplet surface provides the total droplet evaporation rate. Knowing this quantity, as well as assuming the pinning of the contact line and the spherical cap shape of the droplet, the velocity profile of the liquid–air interface was calculated and used in the corresponding boundary conditions.

To discretize and numerically solve this complex system of strongly coupled equations of flow, diffusion, and heat transfer in three phases with temperature-dependent properties, the commercial software COMSOL Multiphysics (www.comsol.com) was used, which implements the finite element method in the weak formulation of the physics equations, and all boundary conditions were implemented in the form of constraints with Lagrange multipliers. Second-order finite elements on a triangular mesh were used for the spatial discretization, and a generalized alpha method was used for the temporal discretization.

The ultimate aim of this modelling is to reproduce the experimentally observable hydrothermal waves and understand their nature and the principles of their development in sessile droplets, whereas the current objective is to numerically model the real experimental conditions, including all relevant physical processes, not only of the liquid droplet, but also of the gaseous phase. The results of a 2D axisymmetric steady-state modelling of a sessile drop of ethanol evaporating into the ambient atmosphere under terrestrial gravity conditions on top of a heated cylindrical substrate are shown in Fig. 20. Two bifurcating branches of the steady-state solutions can be seen. The bifurcation is related to the different flow patterns in the surrounding atmosphere but not in the drop. Both thermal and solutal gravitational vortices, rotating in different directions, are present in the air phase for both branches of stationary solutions. On the other hand, the flow pattern within the drop was the same (one thermo-capillary vortex, as shown in Fig. 21) for the studied range of substrate temperatures (up to 15 °C above the ambient temperature), and did not reveal any flow bifurcations within the droplet. The model showed an agreement with the experimental evaporation rate within a 10% error, which corresponds to experimental error bars.

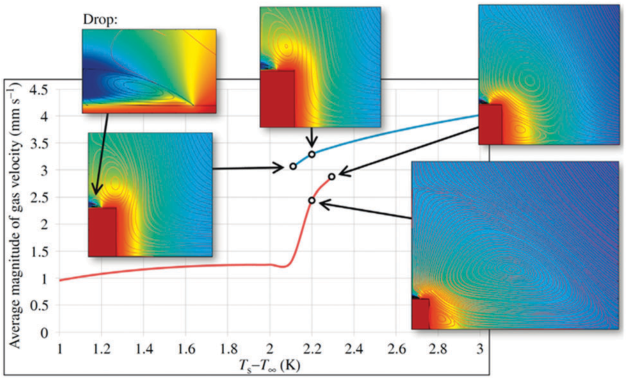

Fig. 20 Axisymmetric steady-state numerical model of a sessile drop of ethanol evaporating into ambient atmosphere under terrestrial gravity conditions on top of a heated cylindrical substrate. The streamlines in the drop and atmosphere indicate the flow field, the colour shows the temperature field, and $T_S - T_{inf}$ is the temperature difference between the substrate and ambient air. Reproduced from ref. 109 with permission from Elsevier, copyright 2015.

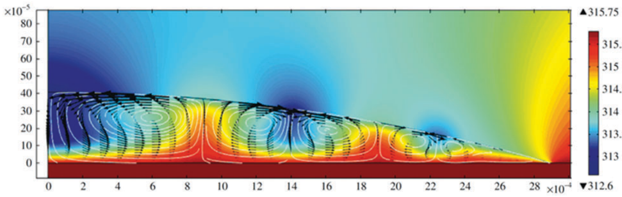

Fig. 21 Two-dimensional axisymmetric unsteady numerical model of a sessile drop of ethanol evaporation in a closed chamber under microgravity conditions on top of a heated substrate. The streamlines and arrows in the drop indicate the flow field, and the colour is the temperature field (in Kelvins). Reproduced from ref. 109 with permission from Elsevier, copyright 2015.

Another 2D axisymmetric numerical model is based on the parabolic flight experiment, that is, a sessile drop of ethanol on top of a heated substrate, evaporating into a closed chamber under microgravity conditions. Because evaporation occurs in a closed chamber, the problem was solved through an unsteady formulation. First, preheating of the substrate and chamber was modelled without drop evaporation, as applied in the real experiment. Next, the drop evaporation starts instantly (the stage of drop injection and spreading is not modelled), and the time-dependent process of evaporation is computed under the condition of a pinned triple line. The results indicate that, after a short transitional stage at the beginning of evaporation, both the numerical and experimental evaporation rates become more or less stable (but not yet steady, and still evolving over time) and agree well with each other. This unsteady model reveals thermo-convective instabilities within the droplet (Fig. 21), which did not appear in the previous equivalent steady-state problem (Fig. 20). From a qualitative point of view, very similar thermo-convective instabilities were obtained using a one-sided unsteady model.[71]

It is interesting to note that using absolutely the same physics as in our unsteady numerical model (parabolic flight experiment with microgravity), but replacing the closed chamber with an open atmosphere, and switching to a steady-state problem formulation, results in a stationary solution with only one thermo-capillary vortex within the droplet, as in the previous steady-state simulation. Even using a multicellular flow structure (Fig. 21) as the initial condition for the steady-state problem results in a stationary solution with one thermos-capillary vortex within the droplet.

Thus, comparing the steady-state and unsteady numerical models, it can be concluded that these two approaches result in a significant qualitative difference in the solutions obtained. The unsteady solution to the problem demonstrates the appearance and development of multicellular thermo-convective instabilities within the droplet, whereas a steady-state approximation is not suitable for such purpose. Therefore, an unsteady approach is always preferable when thermos-convective instabilities are studied. Because the experimentally observed hydrothermal waves in the sessile drops are three-dimensional and not axisymmetric, further developments of two-sided models and their extension into three dimensions is needed for a better understanding of the phenomenon, and both qualitative and quantitative validations of the model against the available experimental data are required.

5. Pattern formation

5.1. Droplets of colloids

Although nanofluids have been widely studied in several scientific communities (physics, biology, chemistry, *etc.*), several questions remain unanswered regarding the pattern formation of colloidal suspension droplets. One important application for nanofluids is inkjet printing,[26] although nanofluids are very promising for application to two-phase heat transfer as well. Using metallic nanoparticles, inkjet printer technologies are evolving to allow the printing of metallic inks on soft substrates for photovoltaic and several other types of applications. These metallic inks are mostly made of silver, and consequently, are very expensive (about $500 per millilitre). To create controlled patterns using inkjet-printing technology, a chain of droplets, the volume of which has been calculated, must create lines of constant diameter following evaporation. The homogeneity of the line thickness is important because it will affect the electrical resistivity of the resulting pattern. If the concentration of nanoparticles is too low, an o-ring pattern will appear, which means that the matter will not have been uniformly deposited on the substrate. If the concentration is too high, the final thickness will exceed a certain point above which the electrical resistivity will no longer change; thus, the nanoparticles, which are extremely expensive, will be wasted. Thus, the search for the optimal concentration that avoids an o-ring formation and consequently enables a uniform deposition by minimizing the amount of nanoparticles is of great interest. Several authors are currently looking at the driving parameters that may lead to such pattern formation.[72] However, because the evaporation of even a pure fluid droplet remains a complex topic, more research is required to understand the evaporation of complex fluids.[59,73,74]

5.2. Droplets of mono-dispersed colloids

The evaporation dynamics of a nanofluid sessile droplet follow the same behaviour as those of pure fluid sessile droplets in the first stages of evaporation. In the very first instant of droplet creation, as soon as the fluid touches the substrate, the droplet spreads to reach its maximum wetting diameter. Although the influence of spreading of nanofluids was observed,[75,76] such influence was not obvious in all experiments conducted in these studies. After a few minutes, a circular deposit is clearly visible at the edge of the drops. The sessile droplet evaporation profile exhibits non-uniformity at the triple line; this non-uniformity leads to a radial flow toward the triple line to compensate for the evaporation loss at the contact line.[64]

Several conditions must be met for the droplets to form a deposition ring on the substrate: first, the solvent must not completely wet the substrate (contact angle larger than 0°); otherwise, the particle deposition will form a layer that tends to crack, following the direction of evaporation. Then, the triple line must pin a major part of the evaporation to initiate a consistent deposition position to accumulate a sufficient number of particles.

Stick slip droplets tend to form irregular concentric rings.[77] This phenomenon, when forced to occur regularly, can be used to form patterns for industrial applications: homogeneous rings with a perfect spatial distribution by means of solid spheres in the droplets[78] and evaporation onto patterned hydrophobic substrates in the form of pillars.[79] As an interesting counter-example, the coffee ring effect can be suppressed using electrowetting.

Nanoparticles other than polystyrene have been used in previous studies. Denkov *et al.*[74] used latex particles. In the case of mixtures of more complex fluids, at low concentrations, Govor *et al.*[75] described the formation of nanoparticle rings following the evaporation of droplets for a liquid matrix of a binary mixture of nitrocellulose, amyl-acetate, and hexane. The authors used 6 nm nanoparticles of $CoPt_3$ at concentrations below 1%, leading to rings measuring 0.6–1.5 μm in diameter. They experimentally observed a phase separation that leads to the formation of a bilayer structure. The $CoPt_3$ nanoparticles located on the contact line assembled along the line. In this case, the accumulation at the drop edge was pronounced.

Conway *et al.*[70] first investigated the influence of particles on the evaporation dynamics of a drop. Using 200 and 750 nm polystyrene beads, the authors observed the formation of an o-ring and a crater for these bead diameters, and monitored the drop height and mass over time. The authors provided a linear normalized model of the drop mass and a normalized model of the drop height using a square-root function. Using 1 μm particles with a disparity of 0.5 to 2 μm, Marin *et al.*[76] demonstrated that the particles that settle first along the contact line of a coffee ring pattern have an ordered, crystalline structure. Toward the centre of the drop, a transition into a disordered particle arrangement was observed. The authors proposed a model that explains many results described in the literature in which large-scale crystalline deposits were observed for particle sizes ranging from 6 to almost 50 nm. In this range of particle sizes, the critical velocity required for a disordered phase is unreachable within the droplet, which explains the absence of a disordered phase. The authors also stated that, apart from the order-to-disorder transition, there are also transitions within the ordered phase, from square to hexagonal packing and *vice versa* (Fig. 22). In an unconfined system, the most efficient packing lattice is a hexagonal compact. However, in the evaporating drop, the particles are confined within a wedge formed by the glass slide on one side and the liquid–air interface with the contact angle on the other. Such confinement indeed leads to a sequence of hexagonal and square packing structures that depend on the most efficient packing for the available space. Indeed, when a new layer is formed, the confinement by the wedge favours square packing. Away from the step edge, the available space increases and allows for a denser, hexagonal packing structure.

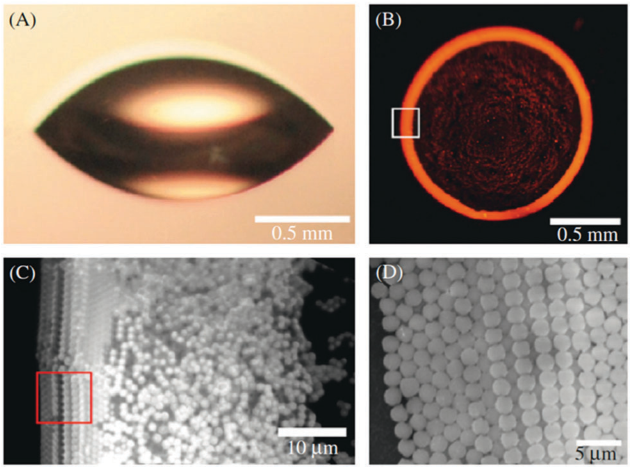

Fig. 22 Order-to-disorder transition in a particle stain left by an evaporating drop. (A) A 3 µL sessile water droplet evaporating from a glass substrate. (B) Ring-shaped stain of red particles (coffee stain) left on the substrate after evaporation. (C) A close-up using an optical microscope of the bottom layer of the stain, taken from the white square in (B), shows that the outermost lines of the stain (left) have an ordered, crystalline structure. Toward the centre of the drop (right), a transition to a disordered particle arrangement is observed. (D) A top view of the ring stain, taken from the red square in (C) using a scanning electron microscope, shows that the first lines of particles (left) are arranged in a hexagonal array, whereas the next lines (brighter in the image) are arranged as a square, followed again by a hexagonal array (references to the colours used in this figure can be found in the online version of this document). Reproduced from ref. 76 with permission from Springer, copyright 2011.

5.3. Droplets of bi-dispersed colloids

O-ring formation during colloidal drop evaporation was first explained by Deegan.[64,65,85] Using sulfate-terminated polystyrene spheres of two sizes, 1 and 0.1 µm, at a maximum volume concentration of 2% dried on glass plates, the author observed the formation of different patterns depending on the concentration and size of the spheres used. For spheres measuring 100 nm and concentrations ranging from 0.063% to 0.25%, Deegan observed the formation of multiple rings for initial droplets measuring 6 mm in diameter. In all cases, particles remained at the drop centre and were not located only at the drop edge. In this study, we observed two different final patterns on the substrate depending on the concentration: an o-ring pattern and a nearly uniform deposition pattern.

Chhasatia and Sun[26] used bi-dispersed colloids made of micro- and nanoparticles, and observed the interaction between these particles and the contact line. For 100 nm and 1.1 µm particles, the authors observed that, at the end of the evaporation process, the nanoparticles were located near the triple line, followed by the microparticles. For a hydrophobic substrate, the constant contact angle mode dominates the evaporation process, leaving little carrier liquid left to rearrang the particles according to their sizes in mixed mode. For a hydrophilic substrate of $0^\circ < \theta < 45^\circ$, particle separation is incomplete during the final deposition. Three separate regions exist from the outer edges to the centre of the drop, including a region with only nanoparticles, a mixture of micro- and nanoparticles, and an inside region with only micro-particles. The width of the middle region where the micro- and nanoparticles overlap depends on the interactions of the surface tension and friction forces acting on the particles. For a hydrophilic substrate of $\theta < 0^\circ$, nanoparticles accumulate at the contact line, forming several rows that prevent the contact line from receding. This enhanced pinning by the nanoparticles permits a radially outward evaporative flow toward the pinned contact line and pushes some of the micro-particles to exceed through the liquid–vapour interface. The reduced surface tension acting on these exceeded micro-particles prevents them from moving inward, whereas most of the other micro-particles move radially inward to the centre of the drop. By modifying the wettability of the substrate, the surface tension acting on the particles is tuned. The control of particle separation according to the particle sizes can therefore be achieved. The authors also found that an increase in the size ratio of the bi-dispersed particles improves the particle separation. Because the number of particles affects the contact line pinning, the boundaries between mixed, partially separated, and completely separated regimes shift toward a higher contact angle for a higher particle loading. By controlling the substrate wettability, particle size ratio, particle loading, and relative humidity, the deposition morphology of bi-dispersed particles can be further controlled.

During the drying of droplets containing latex particles measuring from 40 nm to 5 µm, Monteux and Lequeux[78] observed a rearrangement leading to the formation of rings. The smallest nanoparticles were deposited on the outer side of the ring, whereas the largest particles were located on the inner side. The authors concluded that this deposition mechanism leads to a tight deposition but leaves a thin liquid film of pure water at the edge of the drop. The size of the deposited particle ring can be precisely controlled through a change in the particle size. This segregation effect may consequently play an important role in polymer and biological fluids, which are composed of poly-disperse particles.

5.4. Evaporation kinetics of nano-suspensions of inorganic particles

The evaporation kinetics of relatively large (bigger than 1 µm) sessile droplets of an aqueous suspension of inorganic nanoparticles on solid substrates of various amounts of wettability was investigated from both experimental and theoretical points of view.[86] The following nanoparticles were used: silicon dioxide (SiO_2), titanium dioxide (TiO_2) and carbon nano-powder (C). Two types of carbon nanoparticles were used: carbon nanoparticles with a size of <50 nm (C50) and carbon nanoparticles with a size of <500 nm (C500). The SiO_2 and TiO_2 particles had an average diameter of 10–20 nm and approximately 21 nm, respectively. Carbon nanoparticles were subjected to the annealing procedure at Dr Mattia's laboratory at the University of Bath, UK according to the procedure presented in ref. 87. Three kinds of solid substrates of different wetting properties and different thermal conductivities were used: smooth silicon wafers, ultra-high molecular weight polyethylene films (PE), and polytetrafluoroethylene films (PTFE).

Experimental results on the evaporation of various types of inorganic nano-suspensions on solid surfaces of different hydrophobicity/hydrophilicity were compared with theoretical predictions of the diffusion-limited evaporation of sessile droplets of pure liquids in the presence of contact angle hysteresis discussed above, and very good agreement was found for both evaporation stages (Fig. 7a).

Note that static advancing, θ_{ad}, and static receding, θ_{r}, contact angles cannot be determined independently from the theory used below. That is, these contact angles were taken from the experimental results in ref. 86. It is shown in ref. 86 that the kinetics of evaporation of the above-mentioned aqueous nano-suspensions is in good agreement with the theory developed for pure liquids. The differences from the pure liquids are (i) static advancing and receding contact angles, which are different for each nano-suspension used, and different from the corresponding values for pure water, and (ii) the value of parameter β (eqn (10)). In some cases, two stages of evaporation were observed (stage I and II), whereas in other cases, only stage I was detected.[85]

In Fig. 23, experimental data on the first stage of evaporation are summarised for all nano-suspensions studied in ref. 85. The solid line in Fig. 23 indicates the theoretical prediction. The comparison shows good agreement between the theoretical curve predicted by the theory for pure water and the experimental data. Note that negative values of the dimensionless time for this stage are due to the fact that $\tilde{\tau} = 0$ was arbitrarily selected at $\theta = \pi/2$, and thus negative values correspond to $\theta > \pi/2$. Fig. 24 shows a summary of all nano-suspensions investigated on all solid substrates used, where the evaporation process showed a second stage of evaporation.[86]

Good agreement between the theory predictions for both stages of evaporation (developed for pure liquids) and experimental data on evaporation (within an experimental error range of ±10%) allows the assumption that no adsorption of nanoparticles used occurs in any of the solid surfaces or liquid–vapour interfaces investigated (or the adsorption was negligible); otherwise, a dependency of the receding contact angle on time during the second stage of evaporation would be present. However, we were unable to make such conclusion in these cases, and only the first stage of evaporation was observed.

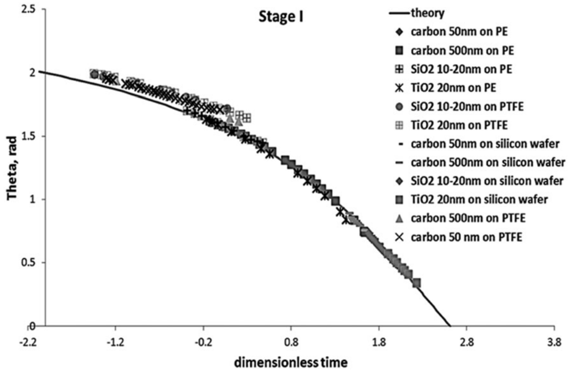

Fig. 23 First stage of evaporation. Summary of all nano-suspensions investigated on all solid substrates used.[86] Reproduced from ref. 86 with permission from APS, copyright 2000.

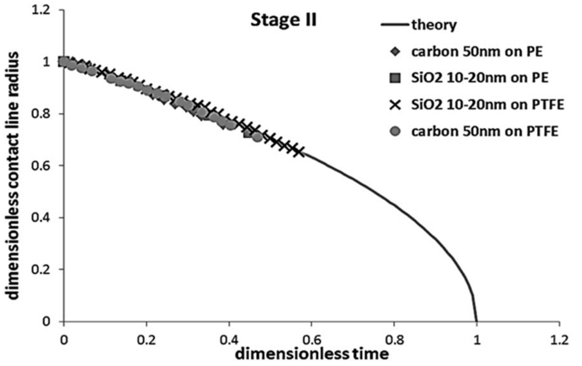

Fig. 24 Second stage of evaporation. Summary of all nano-suspensions investigated on all solid substrates used, where the evaporation process showed the second stage of evaporation.[86] Reproduced from ref. 86 with permission from APS, copyright 2000.

5.5. Pattern formation of nano-suspensions of inorganic particles

After the evaporation process of the nano-suspensions is finished, different patterns are observed on solid surfaces.[5] The pattern formation after evaporation of the suspensions was reviewed in ref. 86 and 5. Below, we add only a few interesting phenomena observed in the case under consideration.[86] According to ref. 86, all nano-suspension pairs of inorganic particles/substrates investigated can be subdivided into two groups: (i) those that evaporated during the first stage only, and (ii) those that evaporated in two stages. Particles accumulated at the centre of the spot, as in the case of C50 on PE (Fig. 25a and b) for the two stages of evaporation, or at the edges, such as TiO_2 on PE (Fig. 25c), when only one stage of evaporation was detected. For case (i), no traceable amount of particles was detected behind the receding three phase contact line. It is shown below that the adsorption of particles (or surfactant) on either a solid–liquid or liquid–air interface results in a deviation from the universal behaviour predicted for pure liquids. The latter shows that nano-suspensions in case (i) did not show substantial adsorption on either interface.

It is impossible to draw any conclusions regarding the adsorption on either interface for the nano-suspensions in case (ii). A theoretical explanation of the observed pattern requires further investigation.

5.6. Droplets of human blood

The evaporation of sessile drops of biological fluid has been studied as a potential area of interest for medical applications.[9] Most studies have been conducted on biological fluids and blood serum, but a few have focused on whole human blood. This chapter summarizes the parameters that influence the evaporation, gelation, cracking, and delamination processes of a drop of whole human blood. It also provides a literature review on the evaporation of biological fluids. Even for this complex fluid, the initial rate of evaporation is well explained using a purely diffusive model of a pure fluid.

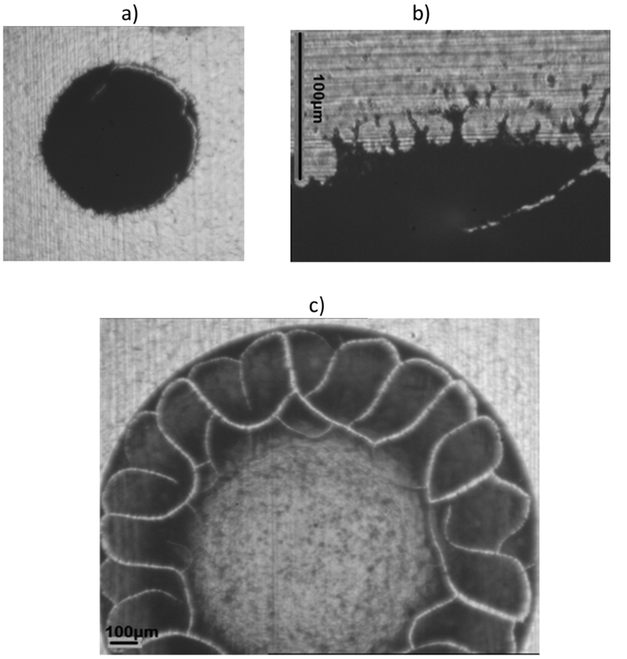

Fig. 25 Microscope images of patterns formed after evaporation of nano-suspensions: (a) C50 on PE, whole spot, (b) magnification of the edge (two stages of evaporation), and (c) TiO_2 on PE (only first stage of evaporation).

Blood is a complex colloidal suspension that behaves like a non-Newtonian fluid. Human blood is composed of different cells that form about 45% of whole blood volume and 25% of the total blood mass.[107] They are classified as red blood cells (RBCs), or erythrocytes; white blood cells (WBCs), or leukocytes; and platelets (thrombocytes). The other 55% is blood plasma, which is composed of water (over 90%), ions, electrolytes (salts), plasma proteins (7%, most of which are by weight), and other substances transported by blood. The main physical properties of whole human blood, such as the density, viscosity, and surface tension, can be found in the literature.[110]

The different stages of blood drop evaporation are shown in Fig. 26.[89] The initial drop diameter presented in the figure is 5.9 mm. The evaporation/desiccation process can be divided into the following five stages. During the evaporation process, the drop is always pinned onto the substrate. The total evaporation time for such case is 36 min, and the durations of the different stages are presented as a percentage of the total time of evaporation.

- Stage 1 (from zero to 20%): The RBCs move out from the centre of the drop to the receding desiccation line. A red deposit is observed at the edge of the drop. The measured speed of the receding desiccation line is 0.7 $\mu m\ s^{-1}$.
- Stage 2 (from 20% to 50%): crystallization appears at the edge of the drop and propagates inward. At the same time, the desiccation process continues from the edge toward the inside of the drop. A dark red torus is observed, which demonstrates a different fluid composition. This torus contains a high concentration of RBCs. These cells are now clearly observed as moving from the centre to the edge of the drop.

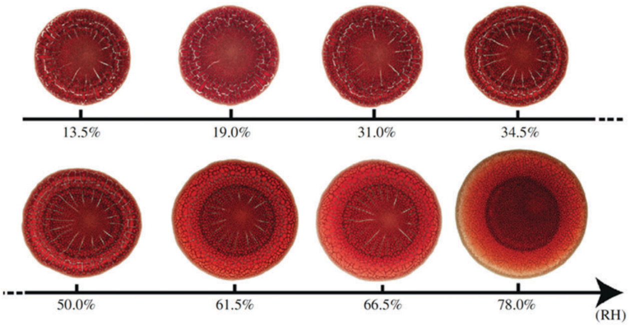

Fig. 26 Top images (identical scale) of deposit left behind after the complete evaporation of a sessile drop of whole blood. All experiments were conducted for an identical drop volume (V = 14.2 μL) and for various ranges of RH (microscope with ultraclean glass substrate, room temperature of 23.8 °C, and room pressure of 1005 hPa). Reproduced from ref. 89 with permission from Elsevier, copyright 2013.

- Stage 3 (from 50% to 70%): the dark red torus desiccates rapidly, and at the same time, the colour of the central part of the drop changes to an increasingly lighter red. The drop is almost totally desiccated, and the first crack appears around the drop between the future corona and central part of the drop.
- Stage 4 (from 70% to 85%): the central part of the drop desiccates, producing much smaller plaque. Desiccation of the corona finishes, and circular drying spots are observed around the corona.
- Stage 5 (from 85% to 100%): the large plaque of the corona moves slightly as soon as it is totally desiccated. This concludes the desiccation of the drop, and no further changes are observed.

All patterns observed with dried drops of blood present similar characteristics: a central part of the drop, wide mobile plaque of the corona with wide white cracks, and a fine periphery. Whereas the central part of the drop and the fine periphery stick onto the glass plate owing to the absence of RBCs, the corona is where mobile deposits form, which do not adhere to the substrate. The explanation of this wetting phenomenon lies in the proteins that exist on the RBCs (glycoproteins). The function of these proteins is to avoid wettability with a wall, and in particular, the internal wall of organs, that is, veins. At the beginning of drop evaporation, the fluid is homogeneous in colloids, which is why a thin periphery can dry on a glass plate. However, because Marangoni convection occurs, the RBCs (and other heavy colloids) accumulate at the triple line, which is receding. The RBCs accumulate through Marangoni convection to form a solid deposit, which is hereafter called the corona. The remaining fluid, which consists mainly of serum without heavy colloids, leads to typical small patterns adhering to the glass substrate after evaporation. One of the parameters that influences the drying rate, and thus the final pattern, is room humidity. The influence of relative humidity (RH) on the pattern at the end of the drying phase has been investigated by considering the same volume of drops of blood evaporating at different RH levels. Final drop images are shown in Fig. 27, which indicate the morphological and structural evolutions of a drying drop of whole blood for different values

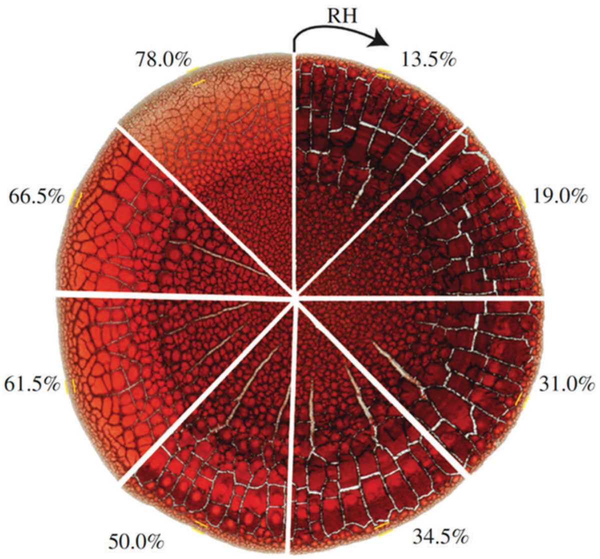

Fig. 27 Final deposition morphology for various RH values (varying between 13.5% and 78.0%). Areas between dashes represent the fine periphery of the corona region. The whole human blood was collected in samples containing liquid anticoagulant.[89] Reproduced from ref. 93 with permission from Elsevier, copyright 2013.

of RH. For each RH, the bottom images are taken at the final evaporation time, t_F, of the drying phase. A structural change, and consequently, the morphological evolutions of the final drying pattern, can clearly be observed. When the evaporation of the blood drop is complete, the final pattern is characterized by the presence of three distinguishable regions: a central part composed of a sticking deposit and a network of small cracks, a corona composed of wide mobile plaque with white cracks organized radially, and a fine periphery completely adhering to the substrate. Fig. 27 shows that the width of the mobile plaque in the corona and the fine periphery region becomes larger as the RH increases. Moreover, the mobile plaque in the corona is more displaced toward the centre of the drop, leaving a wider deposit made of plaque with dark cracks. Fig. 26 also shows that the region of mobile plaque depends on the drying rate. At low drying rates (high RH), more completely adhering mobile plaque is observed than at higher drying rates (lower RH). Indeed, low adhering areas are highlighted by a circular light-red region, which is found in each of the mobile plaque regions within the corona area.

The final drying pattern and crack nucleation vary with the kinetics of the evaporation rate, as presented in Fig. 27. Under our experimental conditions, the transfer of water in the air is limited through diffusion, and is controlled by the RH in the surrounding air. The drying process of a sessile drop of blood is characterized by the evolution of the solution into a gel saturated with solvent. When a gel is formed, the new porous matrix formed by the aggregation of particles continues to dry through evaporation of the solvent that causes the gel to consolidate. As the liquid progressively recedes into the porous medium, it first forms menisci at the air–solvent interface owing to capillary tension between particles, and then forms liquid bridges between these particles. During solvent evaporation, the curvature of the solvent–air menisci is responsible for a capillary pressure in the liquid phase. This depression induces shrinkage of the porous matrix, which is constrained by the adhesion of the deposit to the glass substrate and the evaporation of the solvent. As the tensile stresses build up, the internal stresses become too great, and fractures appear, releasing the mechanical energy. Assuming that gelation is due to particle accumulation, we attribute these differences in pattern formation to the competition between the drying process and the adhesion of the gel on the substrate.

The final dried images shown in Fig. 27 show that the final adhering area of mobile plaque is strongly dependent on the RH. By changing the drying rate, the mechanical properties of the drying gel are modified, such as the adhesion energy of the gel to the glass substrate (according to the Griffith theory). Indeed, the surface area of mobile plaque with drops of blood dried at RH from 13.5% to 50.0% becomes progressively larger with a lower adhering region. This adhering region shrinks until the formation of a circular adhering region leading to a delamination process occurs. For images taken at an RH of above 50%, the mobile plaque is smaller with a higher adhering region. This observation is due to the buckling process that is rapidly overcome by the adhesion of the gel to the substrate. In desiccated colloidal gel dried at RH = 70% and RH = 46%, Pauchard experimentally showed that complete adhesion or de-adhesion is a function of the cell surface area.[104] Moreover, the larger fine periphery of the stick deposited onto the glass substrate owing to the receding of the gel front creates an absence of RBCs, which is due to a change in the internal flow transporting RBCs from the centre to the periphery of the blood drop. The influence of RH on the final drying pattern and on the geometrical parameters was investigated by considering the same small volumes of blood drops evaporating at different RH values.[89] Fig. 28 shows that a linear increase in the contact angle θ_{eq} leads to a decrease in the final wetting diameter D_f of a blood drop as the RH decreases. The higher equilibrium contact angle at higher evaporative rates than at lower evaporative rates can be explained based on the dependence of the dynamic contact angle on the contact line velocity at the moment when the drop touches the glass substrate (at the initial spreading) during the spreading process. Therefore, a large wetting diameter can be attributed to a low equilibrium contact angle. The evaporation of the blood drop can be described using a purely diffusive model by considering the variations in the contact angle and the wetting radius as a function of the RH.

5.7. Spreading of whole blood drop

We now examine the spreading/evaporation dynamics of a blood drop as it touches and subsequently wets a clean glass substrate until its complete evaporation. A pendant-shaped blood drop touching a microscope glass substrate spreads instantaneously until it reaches a final wetting radius and a static advancing contact angle of less than 20°.[102] At the beginning of the evaporation process, the blood drop is homogeneous in bio-colloids. As the drop of blood spreads over the glass substrate, the triple

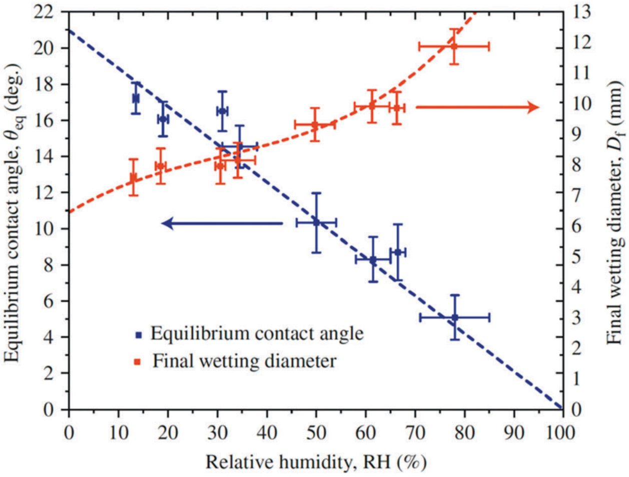

Fig. 28 Variation in the equilibrium contact angle, θ_{eq}, and the final wetting diameter of the blood drop, D_f, as a function of the RH values. The ambient conditions (Ta = 24.5 ± 0.5 °C, Pa = 1005.2 ± 0.6 hPa) and RH vary between 13.5% and 78.0%. The dashed lines indicate a linear fit for the equilibrium contact angle (θ_{eq}) and a cubic fit for the final wetting diameter (D_f) passing by the measurement points. This purely diffusive model shows a good correlation with our experimental results, which decreases with an increase in RH. Reproduced from ref. 89 with permission from Elsevier, copyright 2013.

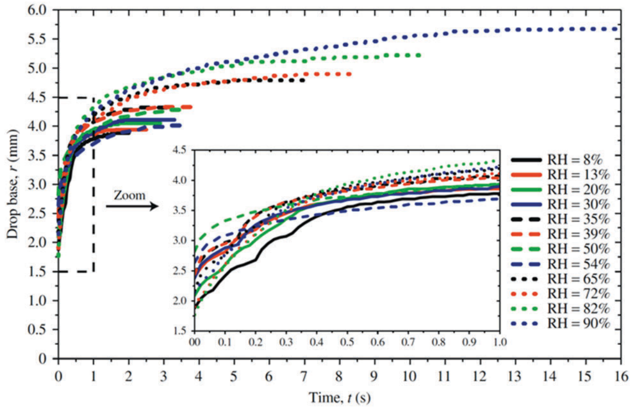

Fig. 29 Evolution of the radius, r, as a function of time, t, for blood drops with viscosity μ = 10.0 mPa s and initial deposited radius (average deposit radius of R_0 = 2.3 ± 0.3 mm) for different humidity levels ranging from 8% to 90%. All experiments were performed for the same drop volume V = 14.2 μL ± 1.0% (average mass m = 13.5 mg ± 9.5%). Ambient conditions (Ta = 25.5 ± 0.5 °C, Pa = 1005.2 ± 0.5 hPa) were used. The inset graph shows a magnification of the spreading time from 0 to 1 s. Reproduced from ref. 102 with permission from Elsevier, copyright 2014.

line moves radially outward with a contact line velocity, U_{CL}, and then becomes pinned to the substrate (evaporation continues in constant contact area mode). In the case of biological fluids, proteins adsorb on the glass substrate near the contact line, which anchors the triple line. Under hydrophilic situations, an internal outward flow develops inside the blood droplet.[89] Subsequently, micrometre-sized colloids (RBCs) accumulate near the contact line, reinforcing the contact line pinning, and thus forming a layer of biological deposits. For a small drop (V = 14.2 μL) with a contact base radius of less than or equal to the capillary length of water, the blood drop retains its spherical cap shape during the entire spreading/evaporation process. Thus, the instantaneous configuration of the drop can be described based on the time-dependent wetting radius, $r(t)$, of the spreading droplet. However, the blood droplets spread faster at higher evaporative rates than at lower evaporative rates (Fig. 29). Consequently, the total spreading time, t_s, increases with an increase in RH values. All curves exhibit the same qualitative behaviour as characterized by the two distinct spreading regimes.

During the experiments, the evaporation occurred in a quasi-steady manner because the diffusion time is much smaller than the time of evaporation, C_v (12 RH)/ρ, which is on the order of 105. In the diffusive-limited case (hydrophilic situation), this evaporative mass flux, J, along the blood drop surface proportional to the vapour concentration difference between the drop surface and the ambient air was not uniform and tended to diverge near the contact line.[103]

For small contact angles, this diverging evaporative flux leads to a diverging velocity field ($u(\rho, \theta) = (1/\rho l)J(\rho)$) because of the singular corner geometry of the droplet close to the contact line.[86,106] The non-uniform evaporation mass flux leads to temperature gradients over the drop surface (self-cooling), which leads to differences in surface tension and drives a Marangoni flow inside the droplet.[88] This internal flow transports the micrometre-sized colloids and liquid toward the rim to replenish the liquid near the contact line, which evaporates significantly faster. The intensity of the rate of evaporation scales with this internal flow motion inside the blood drop. Indeed, an increased rate of evaporation was observed within the vicinity of the triple line at higher evaporative rates (Fig. 30) compared to at lower evaporative rates (Fig. 30). This increase in the evaporation rate enhances the transportation mechanism of the colloids toward the edge of the blood drop and thus increases the flow velocity near the contact line. Consequently, the mean velocity near the contact line decreases with an increase in RH. In the diffusion-limited evaporation case and for low contact angles (θ_{eq} = 20°), the spreading/evaporation process can be divided into two regimes: a fast initial regime,

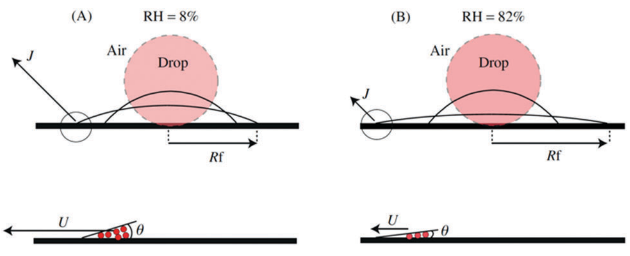

Fig. 30 Schematic representation of spreading drops for the cases of (A) RH = 8% and (B) RH = 82%. Initially, the blood drop has a spherical shape, and at equilibrium, the drop has a spherical cap shape. The arrows indicate the velocity and evaporative flux of water vapour from the drop surface to the surroundings within the vicinity of the triple line. The dashed square marks the area close to the triple line, where the drop geometry can be approximated as a wedge shape. Reproduced from ref. 102 with permission from Elsevier, copyright 2014.

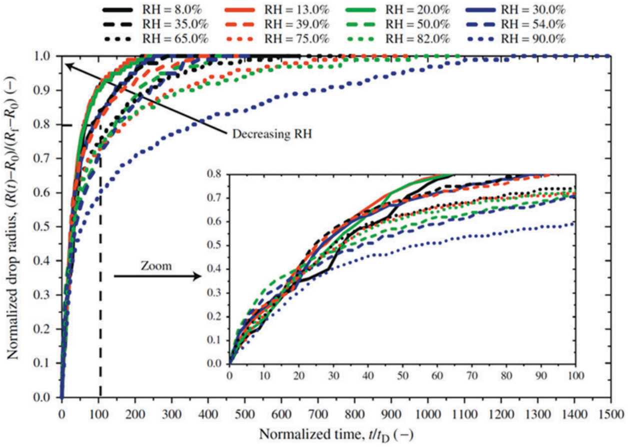

Fig. 31 Normalized drop radius, $r(t) = (r(t)^2R_0)/(R_f{}^2R_0)$, as a function of normalized time, t/t_D, for RH varying from 8% to 90%. The inset graph shows a magnification of t/t_D from 0 to 100. Reproduced from ref. 102 with permission from Elsevier, copyright 2014.

and a slow second regime. In the first regime, the spreading process is controlled through viscous and surface tension forces because all of the experimental radius curves collapse upon one another (Fig. 31). The curves of the spreading radius were scaled by dividing the spreading time by the viscous-capillary characteristic time, $t_D = 4\pi\mu/\gamma R_f$. The radius evolution can be expressed by a power law of the form $r(t) = k(t/t_D)^n$, with a pre-exponential factor $k = 2.193 \pm 1.022$ and a wetting exponent $n = 0.65 \pm 0.11$, and was obtained by fitting the experimental curves. Indeed, the evolution of the wetted drop radius depends on the dominant physical forces driving and resisting the spreading process. It was concluded that $F_{\text{capillary}} > F_{\text{gravity}} > F_{\text{viscosity}} > F_{\text{inertia}}$. Thus, the effects of gravity are negligible, and capillary forces dominate the flow motion inside the blood drop. In this regime, capillary forces rapidly drive the drop spreading because of the curved surface at the contact point (between the drop and the glass substrate), whereas the viscous forces of the fluid resist deformation. The value of the wetting exponent ($n = 0.656 \pm 0.11$) can be explained by the balance of the viscous stress ($B\mu(\mathrm{d}r/\mathrm{d}t)/L$) with the capillary pressure ($\gamma R/r^2$). For a viscosity equal to or larger than 10 mPa s, a wetting exponent of 2/3 was observed in ref. 90 when a viscous-capillary characteristic time $t\mu^5\mu R_0/\gamma$ was used. This shows that bio-colloids inside a blood drop have no significant effect during the early stages of spreading.

Late in the process, the spreading is controlled by the competition between viscous forces (shear-thinning) and by the difference between the saturated pressure at the drop interface and the air pressure because all of the experimental radius curves collapse upon one another (Fig. 31). The curves of the spreading radius are scaled by dividing the spreading time by the evaporation time, t_F. For the second regime of spreading, the radius evolution can be expressed using a power law in the form $r(t) = k(t/t_D)^n$, with a wetting exponent $n = 0.196 \pm 0.03$. From the literature, it is known that the rate of spreading of a shear-thinning fluid is lower than that of a Newtonian fluid ($m = 1$) because of the shearing forces near the moving contact line.[91]

Indeed, the shear-thinning rheology decreases the curvature of the liquid–vapour interface near a moving contact line. Thus, a weaker dependence of the capillary number Ca with the dynamic contact angle, θ_D, appears compared to a Newtonian fluid ($\theta_{DB} = \mathrm{Ca}^{1/3}$). Contrary to these observations for shear thinning fluids, the wetting exponent is found to be 0.19 (which is higher than that of Tanner's law, $n = 0.10$) because blood is a complex colloidal suspension and different physical mechanisms are involved inside the blood droplet in the course of spreading. The second regime of spreading is governed by viscous dissipation near the contact line. However, the calculation of the Bond number (Bo = 1) revealed that the shape of the drops is a hemispherical cap, and that gravitational effects can be neglected. The effect of gravitational forces can lead to acceleration in the spreading ($r \sim t^{1/8}$), and a very small contribution can be added to the internal flow.[66] For low contact angles, the rate of evaporation from the free surface is not uniform and diverges near the contact line. A small temperature gradient develops at the vapour–liquid interface because the surface of the droplet is cooled through evaporation. Thus, a surface tension gradient is generated, which can induce a Marangoni flow.[67]

Consequently, an evaporation-driven Marangoni flow can enhance the spreading rate during the second regime. Another possible mechanism that may be responsible for a spreading enhancement is the disjoining pressure, $\Pi(h)$. This produces a pressure gradient that competes with the capillary pressure and viscous resistance to the flow.[105] This demonstrates that the accumulation of bio-particles near the moving contact line plays an important role in the spreading dynamics because the velocity of the contact line increases rather than decreases.

During the final stage of the evaporation process, complex patterns composed of cracks are formed on the glass substrate. In the experiments, the transfer of water in the air is limited by diffusion, and is therefore controlled by the RH. The evaporation of whole blood drops on glass was investigated in previous studies.[93,106] The authors described the structural evolution of a blood drop leading to the final pattern observed, and analysed the competition between gelation and evaporation.[93] Several physical mechanisms were involved, including a Marangoni flow, crack formation, gelation, and adhesion. In addition, the authors described the different regimes of evaporation kinetics:[89] an initial regime driven by convection, diffusion, and gelation; a transition phase occurring with the complete gelation of the system; and a regime that is only driven by diffusion (the solvent moves through permeation into the porous matrix). For low contact angles ($\theta \ll 90°$) and for pinned contact lines, Hu and Larson[88,92] obtained the evaporation rate of a droplet for any contact angle.

The drying process of a sessile blood drop is characterised by an evolution of the solution into a gel saturated with the solvent. When the gel is formed inside the drop, the porous matrix formed by the aggregation of particles continues to dry through the evaporation of the solvent, which causes the gel

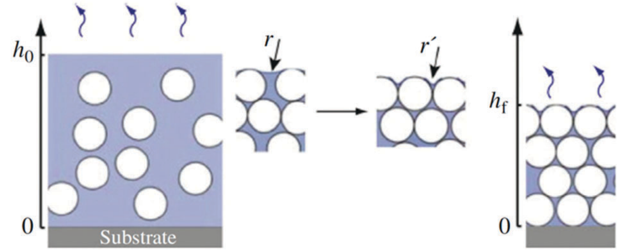

Fig. 32 Formation of a porous matrix during the evaporation process.[89] (left) Particles are dispersed in the solvent. (right) Concentrated suspension of particles (porous matrix) in contact with one another, surrounded by solvent-filled interstices. The system is bounded by two interfaces: the solid–gel interface and the gel–air interface. A curvature of the solvent–air menisci occurs at the evaporation surface and increases during the evaporation process. The competition between adhesion and evaporation leads to a crack formation. Reproduced from ref. 104 with permission from IOPscience, copyright 2006.

to consolidate. Indeed, the system is defined by the two interfaces shown in Fig. 32: the solid–solvent interface and the solvent–air interface. At the latter interface, menisci form, which are responsible for a capillary pressure build-up, P_{cap}, in the liquid phase: $P_{\text{cap}} = \alpha\gamma(s,a)\cdot\cos\theta/r_{\text{p}}$, where $\gamma(s,a)$ is the solvent–air surface tension, r_{p} is the pore radius, and α is a geometrical constant with a value of approximately 10.[94] As the evaporation continues, the curvature of the menisci increases, thereby leading to a depression in the solvent filling in the interstices. However, this depression induces a gradual shrinkage of the porous matrix, which is constrained by the adhesion of the gel to the glass substrate and the evaporation of the solvent. As the tensile stresses build up, the internal stresses become important, and cracks appear, releasing the mechanical energy. However, the dynamics of the cracks depends on the evolution of mechanical stresses and the thickness of the gel layer or deposit. Below a critical thickness, the layer can be free of cracks at the end of the evaporation process.[96]

During the evaporation of a blood drop, a gelled foot forms at the contact line and propagates radially inward, whereas the central area of the blood drop remains in liquid form. As the evaporation continues, this gelled foot leads to the development of ortho-radial constraints in the gel, and thus to the formation of radial cracks. The first cracks nucleate near the contact after the beginning of the evaporation process. Sobac and Brutin[93] conducted experiments on drying blood drops, and observed that these cracks nucleate at a critical particle mass concentration of 29.6%, depending on the initial mass of the drop. After complete evaporation of the blood drop, the final drying pattern is characterised by the presence of four distinguished regions: a central region ($r/R_{\max} < 0.50$) composed of a sticking deposit and a network of small-scale disordered cracks; a transition area ($0.50 < r/R_{\max} < 0.76$) located between the central area and the corona region, which is composed of a network of small and large radial cracks; a corona region ($0.76 < r/R_{\max} < 0.95$) composed of polygonal cells or wide mobile plaque delimited by white cracks; and a fine periphery ($r/R_{\max} > 0.95$), which completely adheres to the solid substrate.

5.8. Droplets of surfactant solutions

The previously developed theory regarding the evaporation of droplets of a pure liquid was applied for an investigation into the kinetics of evaporation of surfactant solutions. In this case, relatively large droplets were considered, that is, the diffusion kinetics of evaporation can be applied.[105]

The kinetics of droplet evaporation of aqueous solutions of SILWET L77 (super-spreader) on a highly hydrophobic substrate was investigated in ref. 100. A buffer of pH 7.0 was used in this study as a solvent to prevent hydrolysis of the SILWET L77. Silicon wafers covered by amorphous Teflon (TEFLON-AF) were used as hydrophobic substrates. The macroscopic contact angle of either pure water or the buffer solution on the substrates was ($118 \pm 2°$). Drops of 4 mm^3 in size were deposited onto the substrate for measurements. Five independent measurements were conducted for each experimental point reported, and the average value was used. The experimental technique applied was similar to that used earlier by Ivanova *et al.*[95,97]

The droplet spreading and evaporation of surfactant solutions demonstrates similar stages to those of pure liquids with partial wetting (Fig. 7a). As discussed in detail by Svitova *et al.*[98] and Ivanova *et al.*,[97] during the spreading process (initial stage) it is possible to use a power-law dependency on time for the contact angle. In experiments presented in ref. 100, the characteristic time scale for the initial stage of spreading was found to be within the range of $t_{\text{ad}} \sim 50$ s. This value is similar to those found in ref. 46 for aqueous trisiloxane solutions. This stage is sufficiently short, that is, less than 100 s, and the volume change is less than 5%;[97] therefore, it is possible to neglect the evaporation during this stage.

In all experiments presented in ref. 95 and 97 (see below), similar to the experiments with pure liquids and nanofluids discussed above, a linear dependence $V^{2/3}(t) = V_0^{2/3} - \text{const}\cdot t$ was found, where $V(t)$ is the dependence of the volume of an evaporating droplet on time (Fig. 33).

It is important to note that the experimental values of both advancing and receding contact angles were used. Such values cannot be predicted within the framework of the above theory.

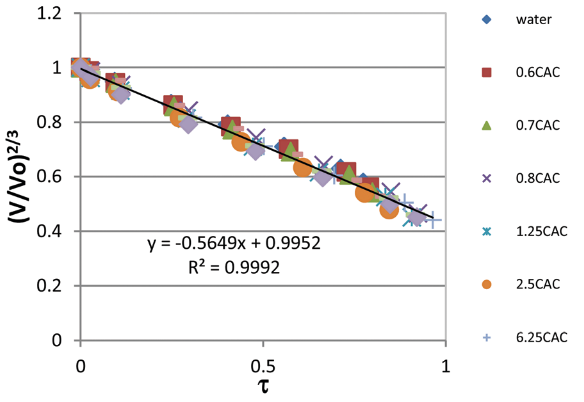

Fig. 33 Experimental dependency of the reduced volume of an evaporating droplet on a reduction of time (equation above) for different SILWET L77 concentrations at an ambient temperature of 24 °C and relative humidity of 50%.

The static advancing contact angle was determined at the beginning of the first stage, when the surfactant concentration was almost identical to the initial concentration. However, the static receding contact angle was determined at the end of the first stage, when the surfactant concentration could be considerably higher when compared with the initial concentration owing to the evaporation. Note that, for concentrations below CWC, the receding contact angle continued to decrease over the entire duration of the second stage of the evaporation process. That is, the actual concentration is different from the initial concentration.

The theoretical predictions for pure water are compared below with the experimental results for aqueous surfactant solutions. Note again that both advancing and receding contact angles and their dependences on the surfactant concentrations were extracted from the experimental data; these angles are very different from those of water. Nevertheless, according to ref. 95 and 97, the kinetics of evaporation of the surfactant solutions is very similar to that of pure aqueous droplets. The main differences in the surfactant solutions are (i) the lower values of the initial contact angles, and as a consequence, (ii) the larger initial radii of the droplet base at all concentrations, and (iii) the dependency of the receding contact angle on time during the second stage at concentrations below CWC.

Fig. 33 confirms that all slopes of $V^{2/3}(t)$ linear dependences are equal to those of pure aqueous droplets within the range of experimental error. It was found in ref. 95 and 97 that the experimental data follow the predicted universal curve during the first stage of evaporation for all investigated temperatures, relative levels of humidity, and concentrations (72 sets of θ, V, and L *versus* t data).

However, the situation is more complex for the second stage of the spreading/evaporation, although agreement with the theory predictions is still rather good. As an example, Fig. 34 shows example data for concentrations below and above CAC obtained at 30 °C and RH of 30%. According to ref. 95 and 97, all other investigated cases show the same behaviour.

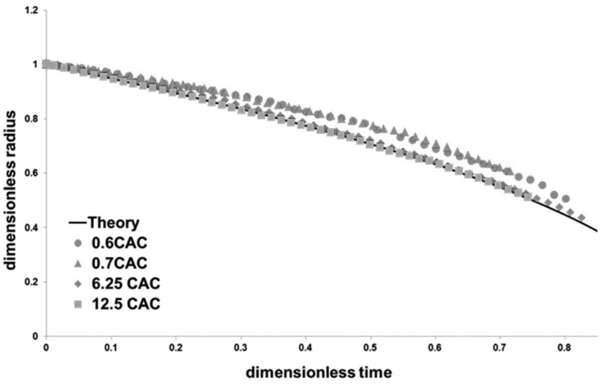

Fig. 34 Comparison of experimental results for SILWET L77 aqueous solutions for the second stage of evaporation with a universal curve predicted based on the theory for pure liquids. Example for relative humidity of 30% and temperature of 30 °C.

It can be seen from Fig. 34 that there is a very good agreement with the theory predictions at concentrations above CAC, and there are deviations from the theoretical predictions at concentrations below CAC. This may be understood when considering that, for $0 < C <$ CAC, the air–liquid and solid–liquid interfacial tensions change as the evaporation progresses owing to the increased concentration. The receding contact angle decreases as the concentration increases within the range of $C <$ CWC. The latter phenomenon was not included in either the computer simulations or the theory above. This may also explain why the agreement between the theory and experiment for pure water is similar to that of the more concentrated surfactant solutions at concentrations of above CWC.

Note again that, to plot the dependences presented in Fig. 34, experimental values of advancing and receding contact angles were used. In Fig. 35, the experimental data published by Doganci *et al.*[99] for their experiments using SDS surfactant (55% RH, 21 °C) are presented along with results for SILWET L-77 (90% RH, 18 °C).[95,97] Fig. 35 shows that the agreement with the theory predictions is similar for both surfactants, although the scattering around the universal curve for the second evaporation stage seems to be higher for the SDS data.

There are two different processes causing the change in surfactant bulk concentration during spreading/evaporation:

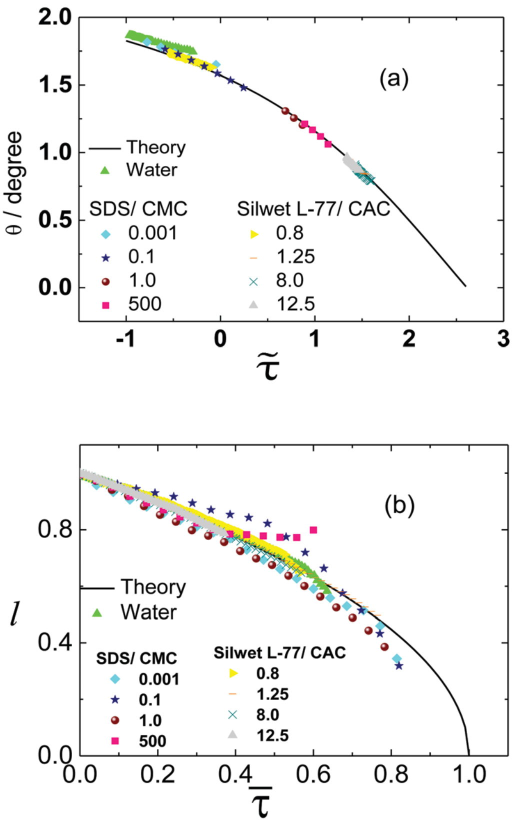

Fig. 35 Comparison of the universal behaviour predicted based on theory for pure liquids, and the experimental results of SDS[98] and SILWET L77[100] solutions for the (a) first and (b) second stages of evaporation. Reproduced from ref. 100 with permission from ACS, copyright 2013.

the concentration (i) decreasing owing to depletion caused by the adsorption, and (ii) increasing because of a decrease of volume owing to evaporation. Estimations made in ref. 95 and 97 have shown that, for the droplet size used, the initial bulk concentration equal to CAC should decrease by about 10% owing to the adsorption at both the liquid–air and liquid–solid interfaces, and about 35% should be adsorbed at the initial bulk concentration of 0.1 CAC. The latter indicates that the adsorption will result in a substantial decrease in bulk concentration inside the droplet, and thus in a significant change in both the advancing and receding contact angles. The evaporation results in an increase in surfactant concentration, and simultaneously, the redistribution between the bulk and interfaces owing to the decrease in droplet volume further affects the value of the receding contact angle. All of these processes have to be taken into account to improve the theory describing the spreading/evaporation of surfactant solutions.

6. Conclusions and outlook

Interest in wetting has increased enormously over the last two decades, particularly since 2010. This growth can be attributed to increasing interest of scientists worldwide to wetting phenomena, which is caused by their wider application to various new areas.

It is therefore impossible to review all publications in this area, which number in the thousands. Thus, we selected the problems investigated by our group over the last decade, and these subjects were reviewed. A review of the current state in the area of simultaneous spreading and evaporation is presented. According to the Kelvin equation, the pendent droplets can only be at equilibrium with an oversaturated vapour. That is, all experiments with droplets are usually used under saturated conditions. This means that evaporation is unavoidable and must be taken into account. This is particularly true if the components of the droplets are volatile liquids. If solutes are also included, steady-state equilibrium can be achieved under sub-saturated conditions once the droplet vapour pressure equals the surrounding partial pressure of the volatilities. We proved that the presence of contact angle hysteresis results in substantially different stages of the spreading/evaporation processes. However, neither static advancing nor static receding contact angles can currently be predicted, and hence, experimental values should be used. In addition, all experimental dependences of the spreading evaporation fall into two universal curves. It was also shown that the stages of kinetics of the spreading/evaporation of nano-suspensions fall into the universal curves when the hysteresis contact angles are determined for these cases. The kinetics of spreading/evaporation of the surfactant solutions were described based on the same universal law during the first stage of spreading/evaporation; however, deviations from the universal behaviour occurred during the second stage, which were caused by changes of the surfactant concentration inside the evaporating droplet over time.

The spreading/evaporation of a blood droplet was also reviewed, and it was shown that the situation is more complicated than with a simple liquid. The residual solids remaining form patterns in the case of evaporation of a nano-suspension; however, these patterns are of an especially complex nature for the case of blood droplets. Possible instabilities and flow pattern formation can be observed in the case of spreading/evaporation. The conditions for these patterns were investigated, along with the flow patterns, using computer simulations. The importance of further investigations into the instabilities arising under microgravity conditions is emphasized. One important outlook of droplet spreading and evaporation is the pattern formation after a complex fluid droplet has dried, which has applications in the industrial inkjet printing of metallic ink. In addition, biomedical applications using whole human blood, blood serum, or even DNA droplets are important areas of study.

Conflicts of interest

There are no conflicts to declare.

Acknowledgements

David Brutin's research was supported by Institut Universitaire de France, Centre National d'Etudes Spatiales, and the European Space Agency. The project leading to this publication has received funding from Excellence Initiative of Aix-Marseille University – A*MIDEX, a French "Investissements d'Avenir" programme. It has been carried out in the framework of the Labex MEC. Victor Starov's research was supported by the Marie Curie ETN grants, MULTIFLOW and CoWet, of the European Science Foundation; the Engineering and Physical Research Council; UK grants EP/J010596/1 and EP/D077869/1; Proctor & Gamble, USA and EU; the European Space Agency under grants FASES, PASTA, and MAP EVAPORATION; and the COST MP 1106 EU project.

References

1 S. Semenov, A. Trybala, R. G. Rubio, N. Kovalchuk, V.r. Starov and M. G. Velarde, *Adv. Colloid Interface Sci.*, 2014, **206**, 382–398.
2 P. Colinet and A. Rednikov, *Eur. Phys. J.: Spec. Top.*, 2011, **197**, 89–113.
3 D. Brutin, Z. Q. Zhu, O. Rahli, J. C. Xie, Q. S. Liu and L. Tadrist, *Microgravity Sci. Technol.*, 2010, **22**(3), 387–395.
4 D. Bonn, J. Eggers, J. Indekeu, J. Meunier and E. Rolley, *Rev. Mod. Phys.*, 2009, **81**(2), 739–805.
5 K. Sefiane, *Patterns from drying drops, Advances in Colloids and Interface Science*, 2014, **206**, 372–381.
6 M. Callies and D. Quere, *Soft Matter*, 2005, **1**, 55.
7 V. Starov, *Adv. Colloid Interface Sci.*, 2010, **161**(1–2), 139–152.
8 S. Hartland, *Surface and interfacial tension measurement, theory, and applications*, Marcel Dekker, New York, NY, Series: Surfactant science series, 2004, vol. 119, p. 1500.

9 V. Starov, M. Velarde and C. Radke, Wetting and Spreading Dynamics, in *Surfactant Science Series*, CRC Press, 2007, vol. 138, pp. 1–544.

10 R. G. Larson, *AIChE J.*, 2014, **60**(5), 1538–1571.

11 V. Starov, Static Contact Angle Hysteresis on Smooth, Homogeneous Solid Substrates, *Colloid Polym. Sci.*, 2013, **291**, 261–270.

12 E. Chibowski, Surface Free Energy of a Solid from Contact Angle Hysteresis, *Adv. Colloid Interface Sci.*, 2003, **103**, 149–172.

13 C. W. Extrand and Y. Kumagai, An Experimental Study of Contact Angle Hysteresis, *J. Colloid Interface Sci.*, 1997, **191**, 378–383.

14 C. W. Extrand, Water Contact Angle and Hysteresis of Polyamid Surfaces, *J. Colloid Interface Sci.*, 2002, **248**, 136–142.

15 E. A. Romanov, D. T. Kokorev and N. V. Churaev, Effect of Wetting Hysteresis on State of Gas Trapped by Liquid in a Capillary, *Int. J. Heat Mass Transfer*, 1973, **16**, 549–554.

16 D. Platikanov, G. P. Yampolskaya, N. Rangelova, Zh. Angarska, L. E. Bobrova and V. N. Izmailova, Free Black Films of Proteins. Thermodynamic Parameters, *Colloid J.*, 1981, **43**, 177–180.

17 N. I. Rangelova, V. N. Izmailova, D. N. Platikanov, G. P. Yampol'skaya and S. D. Tulovskaya, Free Black Films of Proteins: Dynamic Hysteresis of the Contact Angle (Film-Bulk Liquid) and the Rheological Properties of Adsorption Layers, *Colloid J.*, 1990, **52**, 442–447.

18 D. Platikanov, M. Nedyalkov and V. Petkova, Phospholipid Black Foam Films: Dynamic Contact Angles and Gas Permeability of DMPC Bilayer Films, *Adv. Colloid Interface Sci.*, 2003, **101-102**, 185–203.

19 V. M. Starov and M. G. Velarde, Surface Forces and Wetting Phenomena, *J. Phys.: Condens. Matter*, 2009, **21**, 464121.

20 I. Kuchin and V. Starov, Hysteresis of Contact Angle of Sessile Droplets on Smooth Homogeneous Solid Substrates *via* Disjoining/Conjoining Pressure, *Langmuir*, 2015, **31**, 5345–5352.

21 I. Kuchin and V. Starov, Hysteresis of the Contact Angle of a Meniscus inside a Capillary with Smooth, Homogeneous Solid Walls, *Langmuir*, 2016, **32**, 5333–5340.

22 B. V. Derjaguin, N. V. Churaev and V. M. Muller, *Surface Forces*, Consultants Bureau-Plenum, New York, 1987.

23 Z. M. Zorin and N. V. Churaev, *Colloid J.*, 1968, **30**, 371.

24 B. V. Deryagin, I. G. Ershova and N. V. Churaev, *Dokl. Akad. Nauk SSSR*, 1968, **182**, 368.

25 M. M. Viktorina, B. V. Deryagin, I. G. Ershova and N. V. Churaev, *Dokl. Akad. Nauk SSSR*, 1971, **200**, 1306.

26 D. Attinger, Z. Zhao and D. Poulikakos, *Heat Mass Transfer*, 2000, **122**, 544–546.

27 V. H. Chhasatia, A. S. Joshi and Y. Sun, *Appl. Phys. Lett.*, 2010, **97**, 231909.

28 L. Tanner, *J. Phys. D: Appl. Phys.*, 1979, **12**, 1473–1484.

29 R. G. Cox, *J. Fluid Mech.*, 1986, **168**, 195–220.

30 J. Lopez, C. A. Miller and E. Ruckenstein, *J. Colloid Interface Sci.*, 1971, **56**, 460–468.

31 A. M. Cazabat and M. A. Cohen Stuart, *J. Phys. Chem.*, 1986, **90**, 5845–5849.

32 P. Ehrhard, *J. Fluid Mech.*, 1993, **257**, 463–483.

33 D. Duvivier, D. Seveno, R. Rioboo, T. D. Blake and J. De Coninck, *Phys. Rev. E: Stat., Nonlinear, Soft Matter Phys.*, 2011, **27**, 13015–13021.

34 M. J. de Ruijter, J. De Coninck and G. Oshanin, *Langmuir*, 1999, **15**, 2209–2216.

35 P. G. de Gennes, *Rev. Mod. Phys.*, 1985, **57**, 827.

36 V. S. Ajaev, T. Gambaryan-Roisman and P. Stephan, *J. Colloid Interface Sci.*, 2010, **342**, 550.

37 O. Arjmandi-Tash, N. Kovalchuk, A. Trybala, I. Kuchin and V. Starov, Kinetics of Wetting and Spreading of Droplets over Various Substrates, *Langmuir*, 2017, **33**(18), 4367–4385.

38 R. G. Picknett and R. Bexon, *J. Colloid Interface Sci.*, 1977, **61**, 336.

39 F. Girard, M. Antoni, S. Faure and A. Steinchen, *Langmuir*, 2006, **22**, 11085.

40 F. Girard, M. Antoni, S. Faure and A. Steinchen, *Microgravity Sci. Technol.*, 2006, **XVIII-3/4**, 42.

41 F. Girard, M. Antoni, S. Faure and A. Steinchen, *Colloids Surf., A*, 2008, **323**, 36.

42 F. Girard and M. Antoni, *Langmuir*, 2008, **24**, 11342.

43 S. Semenov, V. M. Starov, R. G. Rubio and M. G. Velarde, *Colloids Surf., A*, 2010, **372**, 127.

44 H. Hu and R. G. Larson, *J. Phys. Chem. B*, 2002, **106**, 1334.

45 G. Guena, C. Poulard, M. Voue, J. D. Coninck and A. M. Cazabat, *Colloids Surf., A*, 2006, **291**, 191.

46 S. David, K. Sefiane and L. Tadrist, *Colloids Surf., A*, 2007, **298**, 108.

47 S. Semenov, V. M. Starov, R. G. Rubio and M. G. Velarde, *Colloids Surf., A*, 2010, **372**, 127.

48 F. Schonfeld, K. H. Graf, S. Hardt and H. J. Butt, *Int. J. Heat Mass Transfer*, 2008, **51**, 3696.

49 S. Herbert, S. Fischer, T. Gambaryan-Roisman and P. Stephan, *Int. J. Heat Mass Transfer*, 2013, **61**, 605–614.

50 M. C. Lopes, E. Bonaccurso, T. Gambaryan-Roisman and P. Stephan, *Colloids Surf., A*, 2013, **432**, 64–70.

51 Ch. M. Weickgenannt, Y. Zhang, A. N. Lembach, I. V. Roisman, T. Gambaryan-Roisman, A. L. Yarin and C. Tropea, *Phys. Rev. E: Stat., Nonlinear, Soft Matter Phys.*, 2011, **83**, 036305.

52 P. Kelly-Zion, C. Pursell, N. Hasbamrer, B. Cardozo, K. Gaughan and K. Nickels, *Int. J. Heat Mass Transfer*, 2013, **65**, 165–172.

53 M. Ait Saada, S. Chikh and L. Tadrist, *Int. J. Heat Mass Transfer*, 2013, **58**(1–2), 197–208.

54 P. Zhenhai, D. Susmita, J. A. Weibel and S. V. Garimella, *Langmuir*, 2013, **29**(51), 15831–15841.

55 B. Abramzon and W. A. Sirignano, *Int. J. Heat Mass Transfer*, 1989, **32**(9), 1605–1618.

56 C. Bertoli and M. n. Migliaccio, *Int. J. Heat Fluid Flow*, 1999, **20**(5), 552–561.

57 S. Sazhin, *Prog. Energy Combust. Sci.*, 2006, **32**(2), 162–214.

58 D. B. Spalding, *The Combustion of Liquid Fuel*, Pittsburgh, 1953.

59 P. Kelly-Zion, C. Pursell, S. Vaidya and J. Batra, *Colloids Surf., A*, 2011, **381**(1e3), 31–36.

60 K. S. Lee, C. Y. Cheah, R. J. Copleston, V. M. Starov and K. Sefiane, *Colloids Surf., A*, 2008, **323**, 63.

61 S. Semenov, V. M. Starov, R. G. Rubio, H. Agogo and M. G. Velarde, *Colloids Surf., A*, 2011, **391**, 135.

62 S. Semenov, V. M. Starov, M. Velarde and R. G. Rubio, *Eur. Phys. J.-Spec. Top.*, 2011, **197**, 265.

63 S. Semenov, V. M. Starov, R. G. Rubiob and M. Velarde, *Langmuir*, 2012, **28**, 15203.

64 R. D. Deegan, O. Bakajin, T. F. Dupont, G. Huber, S. R. Nagel and T. A. Witten, *Nature*, 1997, **389**, 827–829.

65 R. D. Deegan, O. Bakajin, T. F. Dupont, G. Huber, S. R. Nagel and T. A. Witten, *Phys. Rev. E: Stat., Nonlinear, Soft Matter Phys.*, 2000, **62**(1), 756–765.

66 H. Hu and R. G. Larson, *Langmuir*, 2005, **21**(9), 3963–3971.

67 H. Hu and R. G. Larson, *Langmuir*, 2005, **21**(9), 3972–3980.

68 K. Sefiane, A. Steinchen and R. Moffat, *Colloids Surf., A*, 2010, **365**(1-3), 95–108.

69 A. Askounis, K. Sefiane, V. Koutsos and M. E. R. Shanahan, *Colloids Surf., A*, 2014, **441**, 855–866.

70 J. Conway, H. Korns and M. R. Fish, *Langmuir*, 1997, **13**, 426–431.

71 S. David, K. Sefiane and L. Tadrist, *Colloids Surf., A*, 2007, **298**, 108–114.

72 J. Xu, J. Xia and Z. Lin, *Angew. Chem., Int. Ed.*, 2007, **46**(11), 1860–1863.

73 F. Fan and K. J. Stebe, *Langmuir*, 2004, **20**(8), 3062–3067.

74 N. Denkov, O. Velev, P. Kralchevski, I. Ivanov, H. Yoshimura and K. Nagayama, *Langmuir*, 1992, **8**(12), 3183–3190.

75 L. V. Govor, G. Reiter, G. H. Bauer and J. Parisi, *Appl. Phys. Lett.*, 2004, **84**(23), 4774–4776.

76 A. G. Marin, H. Gelderblom, D. Lohse and J. H. Snoeijer, *Phys. Rev. Lett.*, 2011, 085502.

77 D. Brutin, B. Sobac, F. Rigollet and C. Le Niliot, *Exp. Therm. Fluid Sci.*, 2011, **35**, 521–530.

78 C. Monteux and F. Lequeux, *Langmuir*, 2011, **27**, 2917–2922.

79 F. Carle, B. Sobac and D. Brutin, *J. Fluid Mech.*, 2012, **712**, 614–623.

80 G. Karapetsas, O. K. Matar, P. Valluri and K. Sefiane, *Langmuir*, 2012, **28**, 11433–11439.

81 B. Sobac and D. Brutin, *Phys. Fluids*, 2012, **24**, 032103.

82 F. Doumenc, T. Boeck, B. Guerrier and M. Rossi, *J. Fluid Mech.*, 2010, **648**, 521–539.

83 P. J. Saenz, P. Valluri, K. Sefiane, G. Karapetsas and O. K. Matar, *Phys. Fluids*, 2013, **25**, 094101.

84 E. Doedel, *J. Franklin Inst.*, 1997, **334B**, 1049–1073.

85 R. D. Deegan, *Phys. Rev. E: Stat., Nonlinear, Soft Matter Phys.*, 2000, **61**(1), 475–485.

86 A. Trybala, A. Okoye, S. Semenov, H. Agogo, R. G. Rubio, F. Ortega and V. M. Starov, *J. Colloid Interface Sci.*, 2013, **403**, 49–57.

87 D. Mattia, M. P. Rossi, B. M. Kim, G. Korneva, H. H. Bau and Y. Gogotsi, *J. Phys. Chem. B*, 2006, **110**, 9850.

88 H. Hu and R. G. Larson, *J. Phys. Chem. B*, 2002, **6**(106), 1334–1344.

89 W. Bou-Zeid and D. Brutin, *Colloids Surf., A*, 2013, **430**, 1–7.

90 D. Legendre and M. Maglio, *Colloids Surf., A*, 2013, **432**, 29–37.

91 A. Carre and F. Eustache, *Heat Mass Transfer*, 2000, **16**, 2936–2940.

92 H. Hu and R. G. Larson, *Langmuir*, 2005, **21**, 3972–3980.

93 B. Sobac and D. Brutin, *Phys. Rev. E: Stat., Nonlinear, Soft Matter Phys.*, 2011, **84**, 011603.

94 C. J. Brinker and G. W. Scherer, *Sol-Gel Science: The Physics and Chemistry of Sol-Gel Processing*, Academic Press, Boston, 1990.

95 H. Ritacco, F. Ortega, R. G. Rubio, N. Ivanova and V. M. Starov, *Colloids Surf., A*, 2010, **365**, 199.

96 S. Bohn, L. Pauchard and Y. Couder, *Phys. Rev. E: Stat., Nonlinear, Soft Matter Phys.*, 2005, **71**, 046214.

97 N. Ivanova, V. M. Starov, D. Johnson, N. Hilal and R. G. Rubio, *Langmuir*, 2009, **25**, 3564.

98 T. Svitova, R. M. Hill and C. J. Radke, *Colloids Surf., A*, 2001, **183–185**, 607.

99 M. D. Doganci, B. U. Sesli and H. Y. Erbil, *J. Colloid Interface Sci.*, 2011, **362**, 524.

100 S. Semenov, A. Trybala, H. Agogo, N. Kovalchuk, F. Ortega, R. G. Rubio, V. M. Starov and M. G. Velarde, *Langmuir*, 2013, **29**(32), 10028–10036.

101 K. Sefiane, *Adv. Colloid Interface Sci.*, 2014, **206**, 372–381.

102 W. Bou-Zeid and D. Brutin, *Colloids Surf., A*, 2014, **456**, 273–285.

103 H. Gelderblom, O. Bloemen and J. H. Snoeijer, *J. Fluid Mech.*, 2012, **12**, 1–16.

104 L. Pauchard, *Europhys. Lett.*, 2006, **74**, 188–194.

105 S. Semenov, A. Trybala, R. G. Rubio, N. Kovalchuk, V. Starov and M. G. Velarde, *Adv. Colloid Interface Sci.*, 2014, **206**, 382–398.

106 B. Sobac and D. Brutin, *Colloids Surf., A*, 2014, **448**, 34–44.

107 M. Thieret, *Biology and Mechanics of Blood Flows, Part II: Mechanics and Medical Aspects*, Springer, New York, NY, 2008.

108 F. Carle, PhD thesis, Aix-Marseille University, 2014.

109 D. Brutin, *Droplet Wetting and Evaporation*, Elsevier, 2015, ISBN: 978-0-12-800722-8.

110 D. Brutin, B. Sobac, B. Loquet and J. Sampol, *J. Fluid Mech.*, 2011, **667**, 85–95.